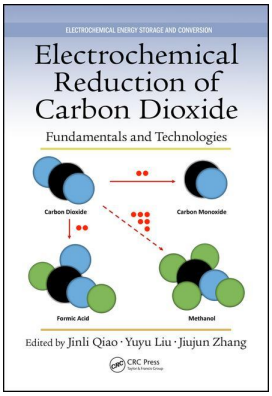


# Electrochemical Reduction of Carbon Dioxide Fundamentals and Technologies

Jinli Qiao, Yuyu Liu, Jiujun Zhang

## Electrochemical Methods for CO Electroreduction

Publication details
https://test.routledgehandbooks.com/doi/10.1201/b20177-6
Jinli Qiao, Yuyu Liu, Jiujun Zhang
**Published online on: 14 Jun 2016**

# 5 Electrochemical Methods for $CO_2$ Electroreduction

*Yu Chen and Dongmei Sun*

## CONTENTS



Electrochemical reduction of carbon dioxide (ERC) provides a means to convert greenhouse carbon dioxide gas to produce diverse attractive chemicals and fuels such as methanol, formic acid, methane, ethylene, carbon monoxide, and other hydrocarbons by using electricity as the source of energy [1] as shown in Equation 5.1. This is attractive because it can be carried out at room temperature and low pressure, and potentially reduces the dependence on foreign fuels as well as mitigates the concentration of $CO_2$ in the atmosphere.

$$CO_2 + xe^{-1} + xH^+ \xrightarrow{eV} CO,\ HCOOH,\ CH_4,\ (HCOOH)_2 \tag{5.1}$$

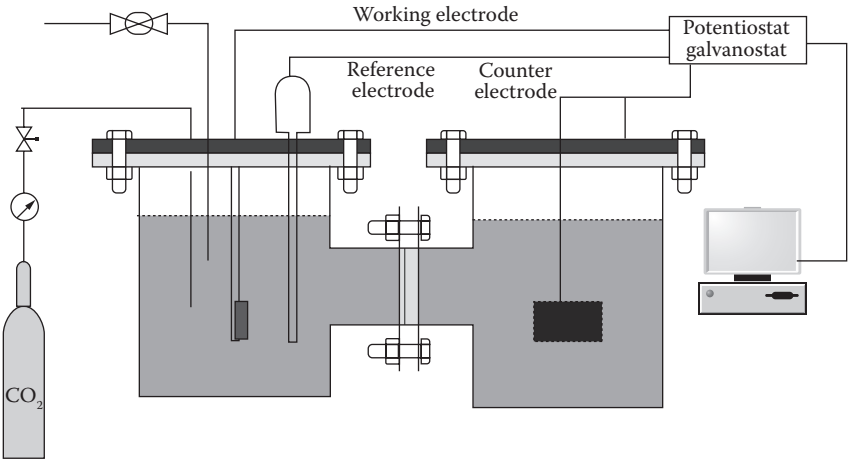


**FIGURE 5.1** Schematic diagram of half-cell assembly. (Reproduced from Hossain, S. *Electrochemical Reduction of Carbon Dioxide to Hydrocarbons*. King Fahd University of Petroleum and Minerals, Saudi Arabia. 2011. With permission from ProQuest ILC.)

Nondestructive techniques, such as cyclic voltammetry (CV), are particularly useful for a first evaluation of the catalyst: determination of the potential at which the catalytic process can be run and of the catalytic efficiency as measured by the current density flowing through the electrode at this potential for a given concentration or partial pressure of the substrate. These techniques may then be used by means of a more detailed kinetic analysis to unravel the mechanism of the catalytic reaction and suggest improvements. Gauging of the selectivity of the catalytic reaction requires moving to preparative-scale electrolysis and determining the faradaic yields of each of the reaction products. Such sustained electrolyses are also necessary to estimate the stability of the catalyst by observing the variation of the preparative-scale current with time. Following the cyclic voltammetric response simultaneously is an additional way of observing the evolution of the catalyst in the course of electrolysis. Preparative-scale evaluation is thus required to establish the actual performances and viability of catalytic systems beyond the rapid test that CV allows.

Alternative methods for ERC investigation include steady-state polarization, linear sweep voltammetry, rotating electrode techniques, electrochemical impedance spectroscopy, and chronoamperometry (CA). Figure 5.1 schematically shows an assembly of a half-cell.

## 5.1 POTENTIOSTATIC OR GALVANOSTATIC STEADY-STATE POLARIZATION

### 5.1.1 Basic Concept

Electrode polarization is defined as the departure of an electrode potential from the equilibrium value upon passage of faradaic current. Current–potential curves under steady-state conditions are called polarization curves. For an ideal polarized

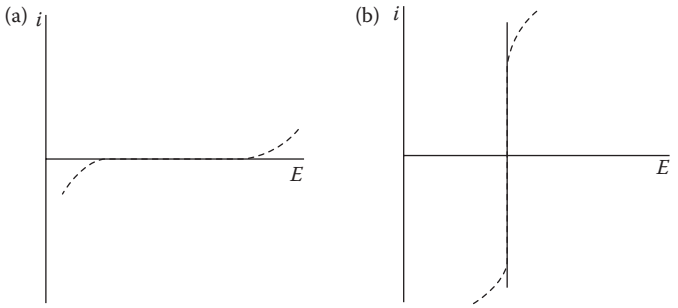


**FIGURE 5.2** Current–potential curves for ideal (a) polarizable and (b) nonpolarizable electrodes. Dashed lines show behavior of actual electrodes that approach the ideal behavior over limited ranges of current or potential. (Bard, A. J. and Faulkner, L. R.: *Electrochemical Methods Fundamentals and Applications*. 2nd edn. p. 22. 2001. Copyright Wiley-VCH Verlag GmbH & Co. KGaA. Reproduced with permission.)

electrode, an infinitesimal current induces a very large change in potential, characterized by a horizontal region of an *i–E* curve (Figure 5.2a). By contrast, for an ideal nonpolarizable electrode, where species is oxidized or reduced at its equilibrium potential value, the potential does not change at all upon passage of current, characterized by a vertical region of an *i–E* curve (Figure 5.2b) [3].

Steady-state polarization curves can be drawn by applying a series of potential/current in a certain step to an electrode, waiting for the response current (potentiostatic)/potential (galvanostatic) to stabilize, and then recording the corresponding data of *i* and *E*.

### 5.1.2 Practical Application for $CO_2$ Electroreduction

Potentiostatic or galvanostatic steady-state polarization is investigated to estimate the efficiency and activity of various $CO_2$ reduction cathodes.

Figure 5.3 shows the simulated steady-state polarization curves in two different $CO_2$-saturated aqueous electrolytes of $KHCO_3$ and $NaClO_4$ both at 0.5 mol/L, where the hydrogen evolution reaction (HER) and CO evolution reaction (CER) were considered separately [4]. As observed, HER always occurs at a more positive potential compared to CER for both electrolytes and all possible reaction, indicating $H_2$ evolution is thermodynamically favored over CO evolution, in good agreement as reflected in the standard potentials. And, there appears obvious positive potential shift either for CO or $H_2$ evolution in $NaClO_4$ solution compared to $KHCO_3$ solution, as the pH value of aqueous $NaClO_4$ is ~3.91, lower than 7.27 of aqueous $KHCO_3$. However, the potential difference at equilibrium for $CO_2$ and $H_2O$ reduction is independent of pH as expected [4].

*In situ* electrodeposited inexpensive Bi catalyst can promote CO evolving (bismuth–carbon monoxide evolving catalyst [Bi-CMEC]) from $CO_2$ over electrochemical reduction with high activity and efficiency as shown in Figure 5.4 over potentiostatic steady-state polarization [5]. A significant lower overpotential compared to inexpensive cathode materials of Cu, Zn, Ni, and stainless steel (SS) is observed,

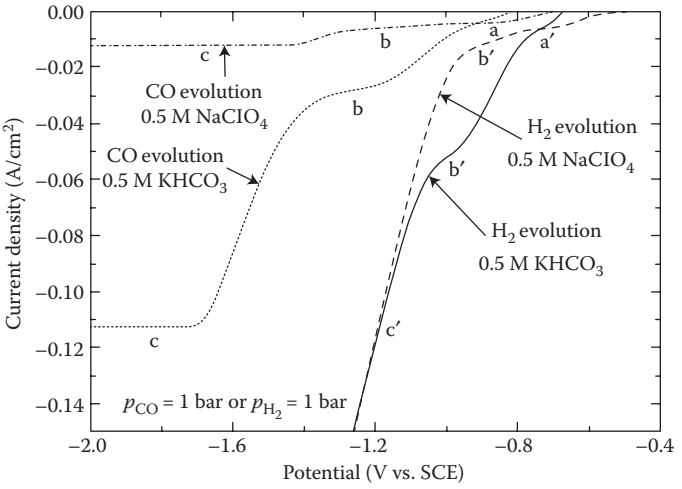


**FIGURE 5.3** Simulated steady-state current density as a function of cathode potential for HER (CER) when it is assumed equilibrated and CER (HER) is discarded ($p_{H_2} = 1$ bar when HER only; $p_{CO} = 1$ bar when CER only; thickness of the Nernst layer = 0.01 cm). (a) $3CO_2 + H_2O + 2e^- \rightleftharpoons CO(g) + 2HCO_3^-$, (b) $4HCO_3^- + 2e^- \rightleftharpoons CO(g) + 2H_2O + 3CO_3^{2-}$, (c) $CO_3^{2-} + 2H_2O + 2e^- \rightleftharpoons CO(g) + 4OH^-$, (a′) $2CO_2 + 2H_2O + 2e^- \rightleftharpoons H_2(g) + 2HCO_3^-$, (b′) $2HCO_3^- + 2e^- \rightleftharpoons H_2(g) + 2CO_3^{2-}$, and (c′) $2H_2O + 2e^- \rightleftharpoons H_2(g) + 2OH^-$. Reactions (a), (b), and (c) and (a′), (b′), and (c′) are written based on the predominate species, as functions of potential. (Delacourt, C., Ridgway, P.L. and Newman, J., *Journal of the Electrochemical Society.* 157(12), B1902–B1910, 2010. With permission from Electrochemical Society.)

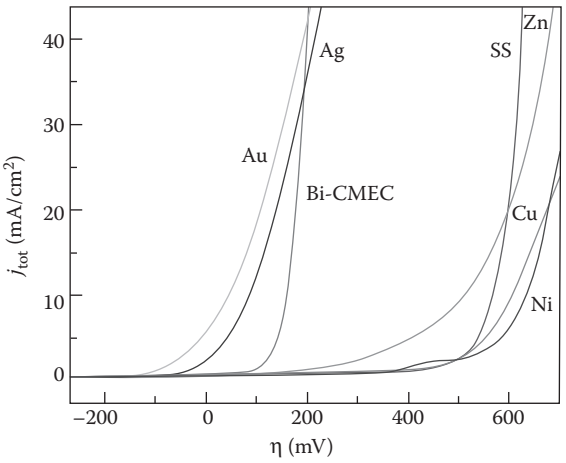


**FIGURE 5.4** Polarization curves recorded for several cathode materials for $CO_2$ reduction in $CO_2$-saturated MeCN with 300 mM [BMIM]OTf. (Reprinted with permission from Medina-Ramos, J., DiMeglio, J. L. and Rosenthal, J. Efficient reduction of $CO_2$ to CO with high current density using *in situ* or *ex situ* prepared bi-based materials. *Journal of the American Chemical Society.* 136(23): 8361–8367. Copyright 2014 American Chemical Society.)

while by contrast similar kinetics and a cathodic half reaction energy efficiency are obtained to that afforded by much more cost-prohibitive Au and Ag electrodes. In addition, the range of the rate of CO production by Bi-CMEC with a surface area of 1.0 $cm^2$ is at ~0.1–0.5 mmol/$cm^2$/h for an applied overpotential of 250 mV.

The current–potential relations for the reduction of carbon dioxide to the formate anion in a neutral solution can be estimated through galvanostatic charging experiments as shown in the polarization curve of Figure 5.5 [6]. From that it is obvious that in region I at low overpotential with a Tafel slope of ~91 mV, the coverage by an adsorbed intermediate, which was suggested to be the formate radical of $HCO_{2ads}$, is large ($\theta \rightarrow 1$), whereas in region II at high overpotential with a Tafel slope of ~240 mV, the coverage is small ($\theta \rightarrow 0$). And for the concentration of carbon dioxide, the reaction order was found to be almost of zero and one in regions I and II, respectively. The reaction mechanism is proposed as follows [7]. In region I of the polarization curve, the rate-determining step is described by Equation 5.4, while in region II, it is the first step described by Equation 5.2.

$$CO_2 + e^- \rightarrow \cdot CO^-_{2ads} \tag{5.2}$$

$$\cdot CO^-_{2ads} + H_2O \xrightarrow{\text{fast}} HCO_{2ads} + OH^- \tag{5.3}$$

$$HCO_{2ads} + e^- \rightarrow HCO_2^- \tag{5.4}$$

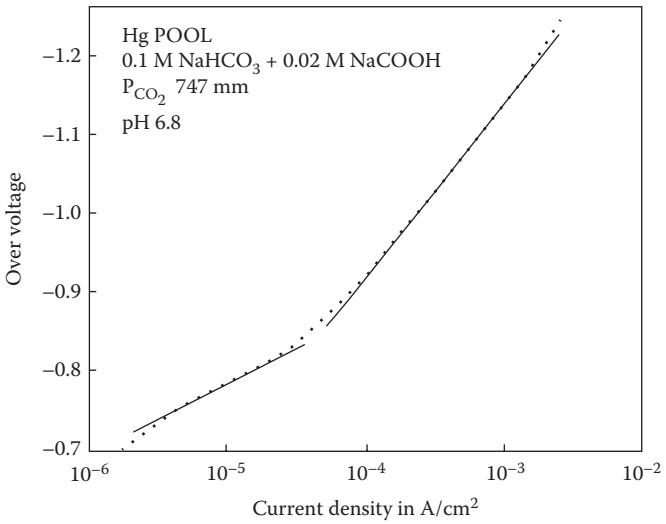


**FIGURE 5.5** Steady-state polarization curve for the reduction of carbon dioxide to the formate anion in a neutral solution. The overvoltage for the reduction of carbon dioxide is obtained by subtracting out the reversible potential which exists for the conditions of the experiment. The curve has been corrected for IR effects. (Reprinted from Russell, P. et al. The electrochemical reduction of carbon dioxide, formic acid, and formaldehyde. *Journal of the Electrochemical Society*. 1977; 124(9): 1329–1338, with permission from the Electrochemical Society.)

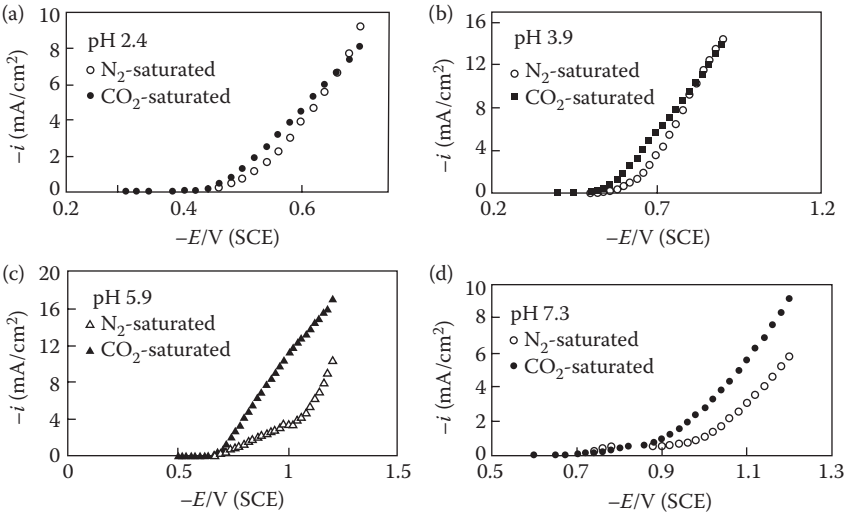


**FIGURE 5.6** Steady-state polarization curves in the absence and in the presence of dissolved $CO_2$ at several values of the pH: (a) pH = 2.4; (b) pH = 3.9; (c) pH = 5.9; and (d) pH = 7.3. (Reproduced from Spataru, N. et al., *Journal of applied Electrochemistry*, 33(12), 1205–1210, 2003. With permission from Kluwer.)

Water may be included in the first step, leading to the formation of $HCO_{2ads}$ [8]. For this case, the first step was the combination of Equations 5.2 and 5.3 [9].

The influence of the pH on the electrochemical reduction of $CO_2$ at the $RuO_2$-coated boron-doped diamond (BDD) electrodes was studied by potentiostatic steady-state polarization as shown in Figure 5.6 [10]. As observed in the pH and potential range investigated, the reduction of carbon dioxide is virtually always accompanied by hydrogen evolution during the whole process of interest. Prior to hydrogen evolution onset, there is no significant $CO_2$ reduction. By comparison, the best efficiency for $CO_2$ reduction can reach 80% for an applied potential of ~−0.55 V at pH 3.9, probably suitable for practical purposes as the pH of a saturated carbonic acid aqueous solution is ~3.7 as well. At pH 5.9, wider potential range for efficient $CO_2$ reduction is achieved, allowing galvanostatic control during electrolysis, which is more convenient than potentiostatic control as usual. At neutral pH (Figure 5.6d), current densities for $CO_2$ reduction are reasonably high, and less affected by hydrogen evolution different from that in acidic media (Figure 5.6a and b) [10].

## 5.2 LINEAR POTENTIAL SWEEP VOTAMMETRY

### 5.2.1 Basic Concept

Linear sweep voltammetry (LSV) is developed to gain more information in a single experiment by linearly sweeping the potential with time at scan rates $v$ ranging from 10 mV/s to about 1000 V/s for conventional electrodes and up to $10^6$ V/s

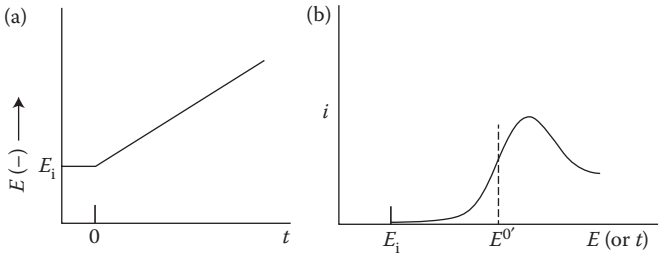


**FIGURE 5.7** (a) Potential scheme as a function of time for linear sweep voltammetry starting at $E_i$. (b) Resulting *i–E* curve. (Bard, A. J. and Faulkner, L. R.: *Electrochemical Methods Fundamentals and Applications*. 2nd edn. p. 227. 2001. Copyright Wiley-VCH Verlag GmbH & Co. KGaA. Reproduced with permission.)

for ultramicroelectrode (UMEs), and recording the *i–E* curve directly. A schematic waveform of the potential applied in a typical LSV is given in Figure 5.7a.

A typical LSV response curve for the reduction of redox active species is shown in Figure 5.7b. At initial electrode potential well positive of $E^{0'}$ for the reduction, only nonfaradaic current flows. When the potential continues to move negatively, the reduction begins at the vicinity of $E^{0'}$ and the current increases with the decrease of the growing potential. As the potential passes $E^{0'}$, the surface concentration of the active analyte drops nearly to zero, and the mass transfer to the electrode surface reaches a maximum rate, and then it declines as the depletion effect sets in, resulting in a peaked current–potential curve as depicted.

For a Nernstian wave, a convenient diagnostic between the peak potential, $E_p$ and half-peak potential, $E_{p/2}$ is expressed by Equation 5.5, Thus, $E_p$ is independent of

$$| E_p - E_{p/2} | = 2.20 \frac{RT}{nF} = \frac{56.5}{n \text{ mV at } 25°C} \tag{5.5}$$

the scan rate. The peak current $i_p$, described by the Randles–Sevčik Equation 5.7 as shown below in Section 5.3, is proportional to $v^{1/2}$, indicating a diffusion-controlled process. A convenient constant of $i_p/v^{1/2}C^*$ depends on $n^{3/2}$ and $D^{1/2}$ and can be used to estimate $n$ for an electrode reaction with a known $n$ value, if a value of $D$ can be estimated [3].

### 5.2.2 Practical Application for $CO_2$ Electroreduction

Linear sweep voltammograms were recorded to determine a potential region of $CO_2$ reduction on a catalyst electrode.

Four post-transition-metal catalysts (Bi, Sn, Pb, and Sb), on glassy carbon or nickel electrodes, drive the formation of CO from $CO_2$ in the presence of [BMIM]OTf differently as shown in Figure 5.8 by LSVs [11]. The onset polarization potentials vary from ~–1.8 to –1.95 V. Of the four electrodeposited catalyst films, the Bi-based cathode shows the earliest onset potential of ~–1.8 V, followed by Sn, and Sb at ~–1.85 V

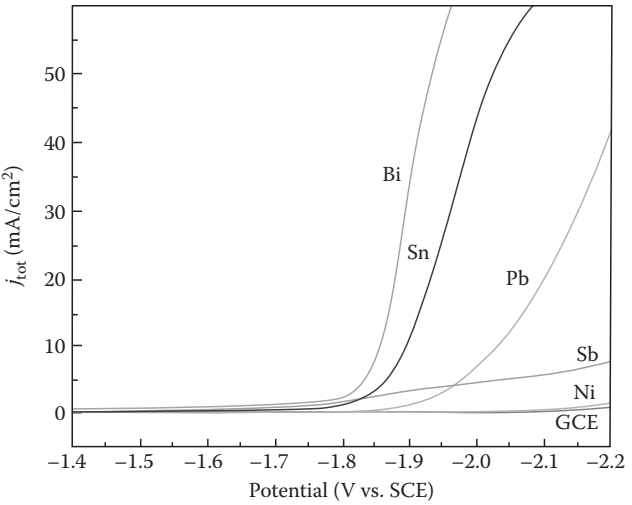


**FIGURE 5.8** Linear sweep voltammograms recorded for electrodeposited cathode materials in $CO_2$-saturated MeCN containing 100 mM [BMIM]OTf. (Reprinted with permission from Medina-Ramos, J. et al. Efficient conversion of $CO_2$ to CO using tin and other inexpensive and easily prepared post-transition metal catalysts. *Journal of the American Chemical Society*. 137(15), 5021–5027. Copyright 2015 American Chemical Society.)

and Pb at −1.95 V. Consequently, Sn and Bi catalysts proved to selectively promote rapid CO evolution with partial current densities of $j_{CO} = 5 - 8$ mA/cm$^2$ at applied overpotentials of $\eta < 250$ mV, whereas the ability of Pb and Sb catalysts to proficient carbon monoxide evolving was poor.

Reductive LSV scans at a reduced nano-$SnO_2$/carbon black coated glassy carbon electrode (Figure 5.9d) in 0.1 M $NaHCO_3$ indicate that the current density for $CO_2$ reduction can reach 6.2 mA/cm$^2$ at −1.8 V, which further increases to as high as 13.1 mA/cm$^2$ under the same conditions when these $SnO_2$ nanoparticles (NPs) were loaded onto graphene. By comparison, both a bare glassy carbon electrode (Figure 5.9a) and carbon black (Figure 5.9b) have negligible catalytic currents for $CO_2$ reduction, whereas electrodeposited ~200 nm tin NPs on glassy carbon provides obvious catalytic reduction current to a density of 3.6 mA/cm$^2$ at −1.8 V for $CO_2$ (Figure 5.9c). The specific current densities (with catalytic currents normalized to the mass of Sn catalysts) were calculated to be 266, 126, and 2 A/g for nano-$SnO_2$/graphene, nano-$SnO_2$/carbon black, and electrodeposited tin NPs, respectively [12].

The molybdenum(Mo)-terminated molybdenum disulfide ($MoS_2$) with abundant metallic-like d electrons in its edge states exhibits superior electrocatalytical activity to $CO_2$ reduction compared with the bulk Ag and Ag NPs (40 nm in average diameter) in $CO_2$-saturated 96 mol% water and 4 mol% EMIM-$BF_4$ solution (pH = 4) as demonstrated by linear sweep voltammetry shown in Figure 5.10a [13]. The $CO_2$ reduction to CO initiates at −0.164 V with faradaic efficiency (FE) at ~3%, suggesting a very low overpotential of 54 mV as the equilibrium potential is at −0.11 V in

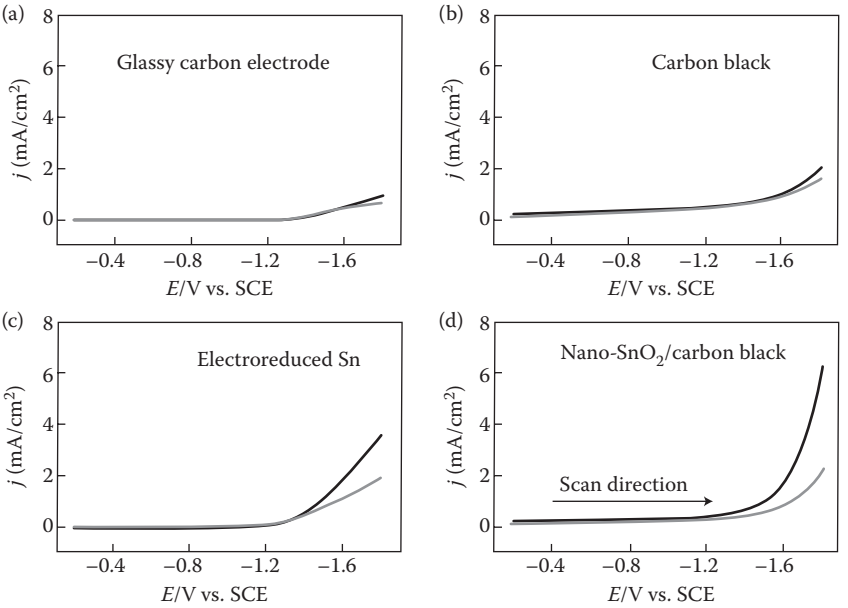


**FIGURE 5.9** (a) Single reductive linear sweep voltammetric scans at 50 mV/s under $N_2$ (gray line) and in a $CO_2$ (1 atm, black line)-saturated solution in aqueous 0.1 M $NaHCO_3$ at a bare glassy carbon electrode (a), glassy carbon electrode with carbon black (b), electrodeposited tin particles (c), and reduced nano-$SnO_2$/carbon black (d). (Reprinted with permission from Zhang, S., Kang, P. and Meyer, T. J. Nanostructured tin catalysts for selective electrochemical reduction of carbon dioxide to formate. *Journal of the American Chemical Society.* 136(5), 1734–1737. Copyright 2014 American Chemical Society.)

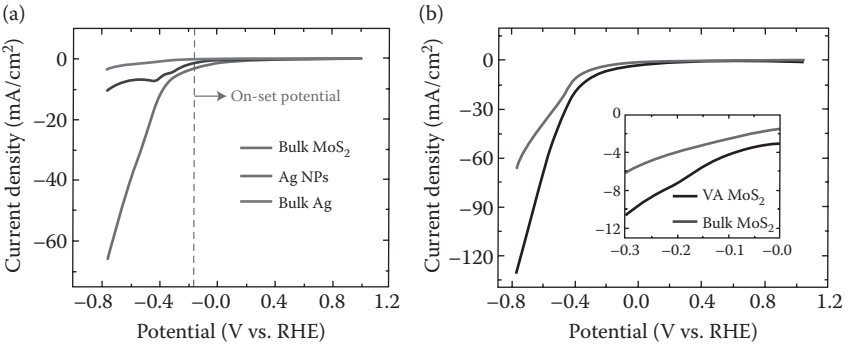


**FIGURE 5.10** (a) Linear sweep voltammetric curves for bulk $MoS_2$, Ag NPs and bulk Ag in $CO_2$-saturated 96 mol% water and 4 mol% EMIM-$BF_4$ solution (pH = 4). The vertical gray line indicates the low overpotential (~54 mV) for $CO_2$ reduction at bulk $MoS_2$. (b) $CO_2$ reduction performance of bulk $MoS_2$ and VA $MoS_2$. (Reprinted by permission from Macmillan Publishers Ltd. *Nature Communications*, Asadi, M. et al. Robust carbon dioxide reduction on molybdenum disulphide edges. 5: 4470, copyright 2014.)

the protic media [14,15]. When the potential increases to −0.764 V, $CO_2$ is selectively converted to CO (FE ~ 98%) at $MoS_2$ with a significantly high reduction current density of 65 mA/cm$^2$, whereas at Ag NPs catalyst with only a current density of 10 mA/cm$^2$ and 65% selectivity, and at bulk Ag with current density of 3 mA/cm$^2$ but for the $H_2$ formation [13]. This is in good agreement with that Mo-edged $MoS_2$ has significantly low work function of 3.9 eV compared to that of the bulk Ag (5.37 eV) and Ag NPs (5.38 eV) [16], indicating that the high current density and low overpotential (54 mV) are mainly due to the metallic character and the high d-electron density of the $MoS_2$ edges. Further study demonstrates that the $EMIM^+$ cation plays a crucial role to high $CO_2$ reduction performance by reducing the reaction barrier for electrons passing into $CO_2$ through *in situ* formation of $[EMIM–CO_2]^+$ complex, which could be adsorbed on the surface of negatively charged $MoS_2$ via coulombic and van der Waals coupling [14,16,17]. In addition, vertically aligned $MoS_2$ (VA $MoS_2$) catalyze $CO_2$ reduction similar to bulk $MoS_2$ in the same experimental condition at low overpotential of 54 mV but with improved performance within complete applied potential range as shown in Figure 5.10b [13]. Two times higher $CO_2$ reduction current density is observed in low potential region for VA $MoS_2$, whereas in high potential region at −0.764 V, a remarkably high current density of 130 mA/cm$^2$ was recorded compared with the bulk $MoS_2$, probably attributed to the high density of active sites preferably Mo atoms available [13].

## 5.3 CYCLIC VOLTAMMETRY

### 5.3.1 Basic Concept

CV is probably the most widely recognized and utilized electrochemical method due to its versatility, nondestructive nature, and rich information that can be extracted relatively quickly, with a wide range of applications in organic and inorganic chemistry as well as materials development. The technique is often employed for initial investigations into prospective catalysts as it is quick and effective at providing useful data regarding electron transfers and allows identification of potentials required for various transformations. It is nondestructive as CV only involves the electrolysis of a small portion of the solution. The current is measured as a potential sweep is applied from an initial potential ($E_i$), generally where no net reaction, therefore minimal current, is expected and the composition of the analyte solution is not affected, to a chosen potential ($E_s$), relevant to the species being investigated. This overpotential can be oxidative or reductive depending upon the nature of the species under examination but is scanned so that the concentration of the redox active substrate concentration at the electrode surface is close to zero, passing through the standard potentials of redox couples studied, $E^0$, where $E_i < E^0 < E_s$. Once $E_s$ is reached, the potential sweep direction is reversed and returned to $E_i$, with any reverse reactions taking place observable in the current response obtained on the reverse sweep. A schematic of the potential waveform used in a typical CV is given in Figure 5.11.

The recorded current response is plotted against the potential to give a cyclic voltammogram, which shows current enhancements and peaks when electrochemical oxidation and reduction take place. An example is given in Figure 5.12.

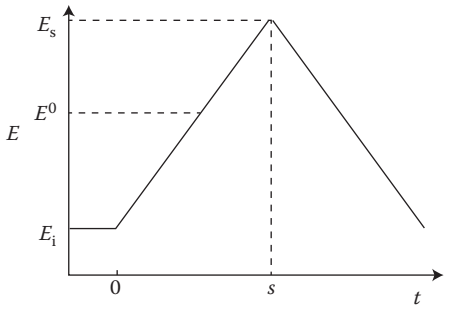


**FIGURE 5.11** Potential scheme as a function of time for CV. (Bard, A. J. and Faulkner, L. R.: *Electrochemical Methods: Fundamentals and Applications.* 2nd edn. p. 227. 2001. Copyright Wiley-VCH Verlag GmbH & Co. KGaA. Reproduced with permission.)

As seen in Figure 5.12, initially, at carefully selected potential of $E_i$, no current flows. However, when the potential is scanned closer to the standard potential of the electrochemical reaction, a current is produced which increases with potential to give a peak, where the maximum current ($I_{pa}$) is observed at the potential of $E_{pa}$ in a nonstirred homogeneous solution containing excess background electrolyte without convection and migration. Upon passing $E_{pa}$, the current response drops. The appearance of the peak is due to mass transport effects, where the movement of the substrate to the electrode surface is limited by the rate of diffusion which is slow compared with the electron-transfer step. Once high-enough overpotentials are applied for the redox process, the concentration of the substrate near the electrode surface drops to zero with the current response decaying as the depletion layer grows. The diffusion

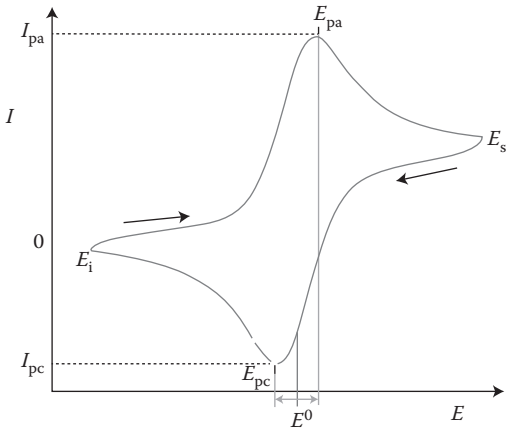


**FIGURE 5.12** Typical reversible cyclic voltammogram. Arrows indicate the direction of the potential sweep. (Bard, A. J. and Faulkner, L. R.: *Electrochemical Methods: Fundamentals and Applications.* 2nd edn. p. 227. 2001. Copyright Wiley-VCH Verlag GmbH & Co. KGaA. Reproduced with permission.)

layer thickness depends upon the experimental timescale but is usually of the order of μm to mm in width, and is the region of solution where the concentration varies from that of the bulk solution [18]. The voltammetric behavior prior to the diffusion limitation is described by the Nernst equation (5.6) [3]:

$$E = E^0 + \frac{RT}{nF}\ln\left(\frac{C_O}{C_R}\right) \tag{5.6}$$

This equation describes the concentration changes near the electrode, with $C_O/C_R$ being the concentration of oxidized/reduced redox species. $E$ is the applied potential, $E^0$ is the standard redox potential, and $R$, $T$, $n$, and $F$ are the ideal gas constant, temperature, number of electrons transferred per molecule, and Faraday's constant, respectively. The logarithmic relationship between the concentration change and potential is responsible for the initial rapid exponential growth in current. Upon reversal of the scan, for an electrochemically reversible system, the opposite processes occur with the product of the forward scan being reduced or oxidized back to the starting material as $E^0$ is reached and exceeded, giving a similar form of current response but of the opposite sign. For a completely reversible process, the ratio of the oxidative and reductive peak currents, $I_{pa}/-I_{pc}$, equals unity. The peak current for diffusion-limited processes is described by the Randles–Sevčik Equation 5.7 below, where the peak current ($I_p$) of a reversible system is dependent on the number of electrons transferred ($n$), the area of the electrode ($A$), the diffusion coefficient ($D$), the concentration of the redox species in the solution ($C$), and the scan rate (ν) [3].

$$I_p = 0.4463\left(\frac{n^3F^3}{RT}\right)^{1/2} AD^{1/2}C\nu^{1/2} \tag{5.7}$$

When standard electrochemical units ($A$ in cm$^2$, ν in V/s, $D$ in cm$^2$/s, and $C$ in mol/cm$^3$) are used at 25°C, the Randles–Sevčik equation can be expressed as

$$I_p = 2.69\times10^5 n^{3/2} AD^{1/2}C\nu^{1/2} \tag{5.8}$$

The degree of reversibility can be assessed using CV through evaluation of the potentials as well as currents observed. If the peak separations of a redox couple increase with scan rate, this is indicative of quasi-reversible kinetics. If however the peaks associated with the forward and backward processes have no overlap on the potential axis or, as found for chemically irreversible processes there is a complete absence of a back-peak, the electron transfer is irreversible. The peak separation of a reversible one-electron process at 25°C is ~59 mV and independent of the scan rate. If $n$ electrons are transferred, the separation is described by Equation 5.9 [19]:

$$\Delta E = E_{pa} - E_{pc} = 2.218\frac{RT}{nF} \tag{5.9}$$

The rate of electron transfer between the electrode and substrate, $k_f$, can be evaluated via voltammetry as it also shows a potential dependence, as described by the Butler–Volmer relation, Equation 5.10 [20]:

$$k_f = k^0 e^{[-(\alpha nF/RT)(E-E^0)]} \tag{5.10}$$

where $k^0$ is the standard heterogeneous rate constant and $\alpha$ is the transfer coefficient. The transfer coefficient represents the sensitivity of the transition state to the shift in potential upon moving from the electrode reactant to the product with possible values 0–1. In electron transfers without significant structural changes or alteration in solvation, this value is ~0.5 [20].

### 5.3.2 Practical Application for $CO_2$ Electroreduction

Cyclic voltammograms are recorded at the Pt/C-based membrane electrode using a single cell equipped with a reference electrode of dynamic hydrogen electrode (DHE), to investigate the $CO_2$ reduction reaction as shown in Figure 5.13 [21]. Under the $CO_2$ atmosphere, there appear three characteristic peaks, designated as regions 1, 2, and 3, where region 1/2 located at 0.06–0.30 V versus DHE, the same as that under the $N_2$ atmosphere, corresponds to H-adsorption/desorption [22]. It is worth noting that the reduction current in the H-adsorption region under the $CO_2$ atmosphere is almost as high as that under the $N_2$ atmosphere, whereas the H-desorption current under the $CO_2$ atmosphere is much lower than that under the $N_2$ atmosphere. And a new peak in region 3 was observed under the $CO_2$ atmosphere. These results indicate that the $CO_2$ reduction occurs in region 1, competing with the H-adsorption reaction. And the product or intermediate of $CO_2$ reduction can be reoxidized in region 3 [21].

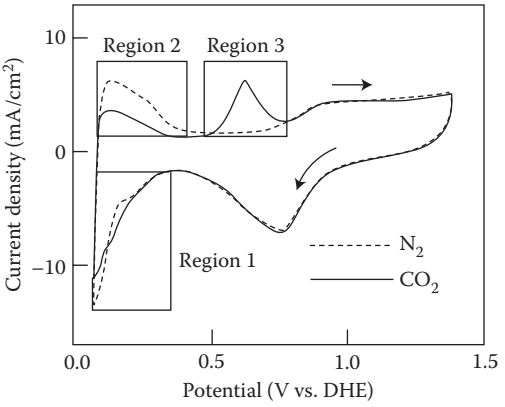


**FIGURE 5.13** Cyclic voltammograms obtained under $N_2$ (dotted line) and $CO_2$ (solid line) atmospheres for the Pt/C-based membrane electrode. Cell temperature: 40°C, scan rate: 10 mV/s. (Reprinted from *Journal of Power Sources,* 228(0), Shironita, S. et al., Feasibility investigation of methanol generation by $CO_2$ reduction using Pt/C-based membrane electrode assembly for a reversible fuel cell, 68–74, Copyright 2013, with permission from Elsevier.)

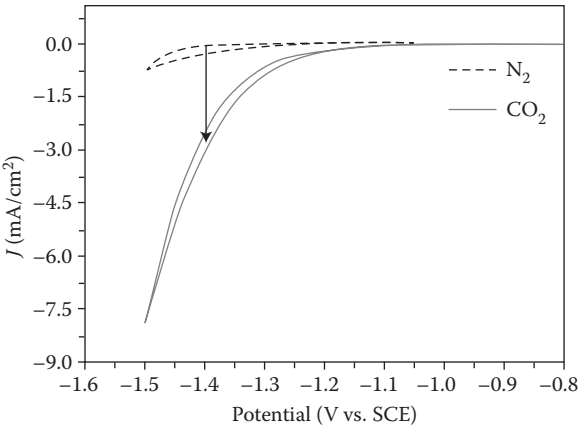


**FIGURE 5.14** Cyclic voltammograms of the $Cu_3Pt$ catalyst recorded in $N_2$- and $CO_2$-saturated 0.5 M $KHCO_3$ with a scan rate of 10 mV/s between −0.8 and −1.5 V (vs. SCE). (Guo, X. et al. Composition dependent activity of Cu–Pt nanocrystals for electrochemical reduction of $CO_2$. *Chemical Communications*. 2015; 51(7): 1345–1348. Reproduced by permission of The Royal Society of Chemistry.)

The $Cu_3Pt$ nanocrystal [23] ($Cu_3Pt$ NC with atomic ratio of Cu:Pt = 3:1) exhibited excellent catalytic activity toward $CO_2$ reduction as shown in Figure 5.14 over CV. It is observed that the reduction current in $CO_2$-saturated solution is much higher than that of a competing process of hydrogen evolution reaction in $N_2$-saturated solution, which strongly indicates that the reduction process is dominated by $CO_2$ reduction and the presence of $CO_2$ seems to inhibit the HER at potentials lower than −1.1 V. The current density of $CO_2$ reduction outcompeting HER could be simply calculated by subtracting the current density obtained at the dashed lines (HER current) from that recorded at the solid lines (the overall current of HER and $CO_2$ reduction), as inferred by the arrow lines in the figures. The onset potential is ~−0.972 V and the $CO_2$ reduction current density is ~0.598 mA/cm$^2$ at −1.3 V versus saturated calomel electrode (SCE).

Metal-free carbon nanofibers (CNFs) catalyst for $CO_2$ electroreduction was examined by CV in pure ionic liquid of EMIM-$BF_4$ by sweeping the applied voltage from 0.79 to −1.14 V versus SHE as shown in Figure 5.15 [24] compared to carbon film (C film) which neither possesses the overall porosity of CNFs nor the fractal-like corrugations characteristic of the individual fibers in CNFs. As observed in CV, in the presence of $CO_2$ for CNFs, a peak appears at −0.573 V, characteristic of the $CO_2$ reduction, similar to that for Ag-induced $CO_2$ reduction [16,17,25]. The calculated FE at −0.573 V is about 98% for CO formation by analyzing the collected products via gas chromatography. Compared with C film, the onset potential for $CO_2$ reduction in CNFs at about 0.23 V is more positive, indicating a smaller overpotential, which is similar to the smallest overpotential reported so far recorded by the Ag catalyst (0.17 V) [14]. Next, the current density at −0.573 V for CNFs is almost two times higher than that for the C film, indicating excellent reduction efficiency of CNFs catalysts, contributed to the high positive charges and spin density of the carbon

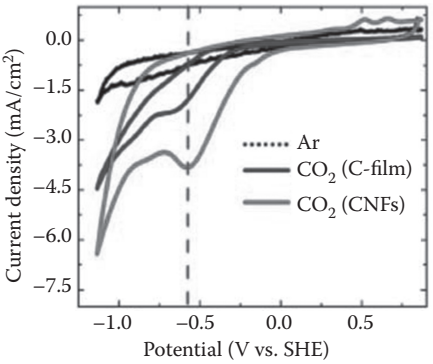


**FIGURE 5.15** CVs for $CO_2$ reduction in Ar-saturated and $CO_2$-saturated pure EMIM-$BF_4$ at 10 mV/s on carbon film electrode (black curve) and CNFs electrode (gray curve), respectively. The vertical dashed line represents the potential at which highest $CO_2$ reduction in the CNFs. (Reprinted by permission from Macmillan Publishers Ltd. *Nature Communications*, Kumar, B. et al. Renewable and metal-free carbon nanofibre catalysts for carbon dioxide reduction. 4, copyright 2013.)

atom around the electronegative nitrogen atom. The naturally oxidized carbon atom, acting as an effective active site, is incessantly renewable during the $CO_2$ electrocatalytic reduction process, resulting in stable current density even after 9 h [24].

The molecular electrocatalyst of $[Ni(cyclam)]^{2+}$ toward homogeneous reduction of $CO_2$ in acetonitrile (ACN) with or without water under $N_2$ and $CO_2$ is studied by CV as shown in Figure 5.16 [26]. As observed, in ACN without water, with the addition of $CO_2$, the Ni(II)/Ni(I) redox couple becomes irreversible and the reduction peak has a slight increase in current and is shifted positively by 30 mV. The positive shift is due to $CO_2$ binding to Ni(I). The irreversibility may arise from a fast, irreversible chemical step of an isomerization [27], following $CO_2$ binding. Interestingly, reversibility of the Ni(II)/Ni(I) couple is regained with scan rates above 3 V/s, assuming that with faster scan rates the chemical step of isomerization cannot proceed because the Ni(I) metal center is reoxidized to Ni(II) before the system can reach equilibrium. With a reversible couple, the $CO_2$ binding constant ($K_{CO_2}$) can be calculated from the shift in the Ni(II)/Ni(I) couple ($\Delta E$) under $N_2$ and $CO_2$ and Equation 5.11 [28]:

$$K_{CO_2}[CO_2] = e^{\Delta E(nF/RT)} - 1 \tag{5.11}$$

Using this electrochemical determination method, $K_{CO_2}$ was found to be 6 $M^{-1}$. Information about the rate of the chemical step following $CO_2$ binding can be obtained as well. The half-life ($t_{1/2}$) is estimated to be ≈0.2 s under these conditions. By contrast, in ACN with water as the proton source, the reversibility is lost even at higher scan rates, suggesting that the chemical step responsible for irreversibility is most likely protonation of the $CO_2$ adduct. As shown in Figure 5.16b, two catalytic peaks develop. The first catalytic peak, a, simultaneously increases in

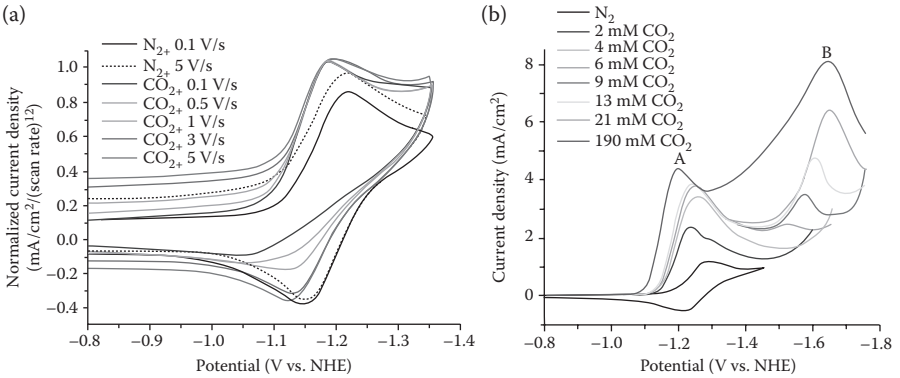


**FIGURE 5.16** (a) Cyclic voltammograms of 1 mM [Ni(cyclam)]$(PF_6)_2$, 0.1 M $TBAPF_6$ in ACN. Current normalized by square root of scan rate. (b) Cyclic voltammograms of 5 mM [Ni(cyclam)]$(Cl)_2$, 0.1 M $TBAPF_6$ in 1:4 water:ACN. Adding $CO_2$ with flow meter. The positive scan portion has been removed for clarity. Scan rate = 0.1 V/s. (Reprinted with permission from Froehlich, J. D. and Kubiak, C. P. The homogeneous reduction of $CO_2$ by [Ni(cyclam)]+: Increased catalytic rates with the addition of a CO scavenger. *Journal of the American Chemical Society.* 137(10), 3565–3573. Copyright 2014 American Chemical Society.)

current density and shifts positively in potential with increasing amounts of water, suggesting a proton-dependent electron transfer. The second reduction occurs only after protonation of the $CO_2$ adduct [29]. The current in peak b is assumed to be, in part, the reduction of a $[Ni(cyclam)(CO)]^+$ species [29] produced by reaction of $[Ni\text{-}(cyclam)]^+$ with CO. Additional contributions to the current in b could also be from $CO_2$ or proton reduction by a Ni(0) species or at the electrode. By varying the $CO_2$ concentration, the first catalytic peak, a, quickly reaches a plateau as the $CO_2$ concentration exceeds that of the catalyst, suggesting that $CO_2$ binding is not a rate-limiting step at high $CO_2$ concentrations. Peak b begins to appear at $[CO_2] > 5$ mM, which is probably related to $CO_2$ reduction by a species other than $[Ni(cyclam)]^+$. The catalytic current under excess $CO_2$ and proton source remains peak shaped, implying that substrate consumption is not the cause of the peak shape but is most likely due to an inhibition process such as catalyst degradation.

The CV of [Mn(mesbpy)-$(CO)_3$(MeCN)](OTf) in dry MeCN without added weak Brønsted acid of MeOH under $N_2$ consists of one couple of reversible reduction peaks at −1.55 V versus $Fc^+/Fc$ with peak-to-peak separation of 39 mV (Figure 5.17a). This redox couple is best described as an electrical equivalent circuit (EEC) mechanism, where two one-electron reductions occur followed by the loss of a MeCN ligand [30]. The second of the two one-electron reductions occurs either at the same or at a lower potential than the first reduction [31]. This overall two-electron reduction leads to the anionic state, $[Mn(mesbpy)(CO)_3]^-$. No CV signal change was observed when the electrochemical solution was sparged with $CO_2$ in dry MeCN. However, once weak Brønsted acid of MeOH was added under $CO_2$, a current increase appeared at ~−2.0 V versus $Fc^+/Fc$, that is, ~400 mV after the two-electron reduction, solely due to the electrocatalytic reduction of $CO_2$ to CO. By contrast, no current increase

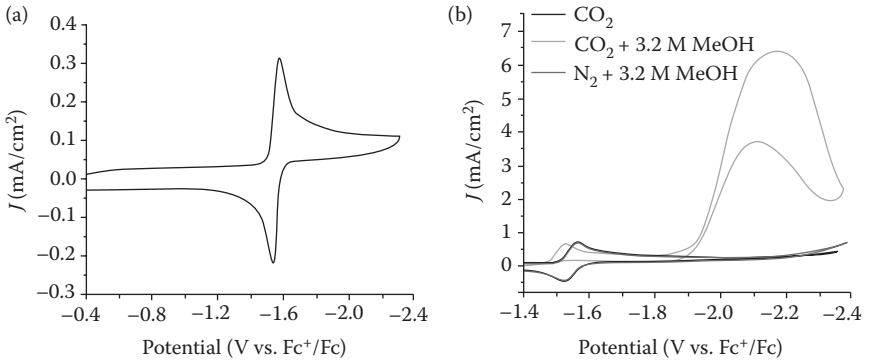


**FIGURE 5.17** (a) Cyclic voltammogram of 0.7 mM [Mn(mesbpy)-$(CO)_3$(MeCN)](OTf) in MeCN with 0.1 M $TBAPF_6$ under $N_2$ at 100 mV/s. (b) Cyclic voltammograms of 1 mM [Mn(mesbpy)$(CO)_3$(MeCN)](OTf) in 0.1 M $TBAPF_6$/MeCN under $CO_2/N_2$ with/without MeOH at 100 mV/s. Scan rate = 0.1 V/s. (Reprinted with permission from Sampson, M. D. et al. Manganese catalysts with bulky bipyridine ligands for the electrocatalytic reduction of carbon dioxide: Eliminating dimerization and altering catalysis. *Journal of the American Chemical Society*. 136(14), 5460–5471. Copyright 2014 American Chemical Society.)

was observed under $N_2$ with added weak acid, indicating that the current increase is not due to proton reduction (Figure 5.17b). Higher concentrations of weak Brønsted acid in $CO_2$ reduction electrocatalysis experiments resulted in increased current densities, before reaching a peak current density and leveling off or dropping with addition of more $H^+$ [30]. For a reversible electron-transfer reaction followed by a fast catalytic reaction ($E_RC_{cat}$ scheme), the peak catalytic current ($i_{cat}$) is given by Equation 5.12 [32]:

$$i_{cat} = n_{cat}FA[\text{cat}](Dk_{cat}[Q]^y)^{1/2} \tag{5.12}$$

assuming that pseudo-first-order kinetics apply; that is, the reaction is first order in catalyst and that the concentrations of the substrates $Q$ are large in comparison to the concentration of the catalyst. In Equation 5.12, $n_{cat}$ is the number of electrons required for the catalytic reaction ($n_{cat} = 2$ for the reduction of $CO_2$ to CO), $F$ is Faraday's constant, $A$ is the surface area of the electrode, [cat] is the catalyst concentration, $D$ is the diffusion constant of the catalytically active species, $k_{cat}$ is the rate constant of the catalytic reaction, and $[Q]$ is the substrate concentrations. At high $[H^+]$, the electrocatalytic reduction of $CO_2$ is first order in the catalyst, first order in $CO_2$, independent of acid concentration, and at steady-state conditions [30]. Equation 5.13 describes the peak current of a complex with a reversible electron transfer and with no following reaction [33]:

$$i_p = 0.4463n_p^{3/2}FA[\text{cat}]\left(\frac{F}{RT}\right)^{1/2}v^{1/2}D^{1/2} \tag{5.13}$$

In Equation 5.13, $i_p$ is the peak current under $N_2$ with an amount of weak Brønsted acid corresponding to peak $i_{cat}$ conditions. $R$ is the universal gas constant, $T$ is the temperature, $n_p$ is the number of electrons in the reversible, noncatalytic reaction, and $\upsilon$ is the scan rate (0.1 V/s). Dividing Equation 5.12 by Equation 5.13 allows the determination of $i_{cat}/i_p$ and allows further calculation of the catalytic rate constant ($k_{cat}$) and the turnover frequency (TOF), as shown in Equation 5.14 [30]:

$$\text{TOF} = k_{cat}[Q] = \frac{Fvn_p^3}{RT}\left(\frac{0.4463}{n_{cat}}\right)^2\left(\frac{i_{cat}}{i_p}\right)^2 \tag{5.14}$$

assuming that the diffusion constant of the catalytically active species does not change significantly under $CO_2$ or $N_2$. Addition of MeOH ($pK_a$ of 29.0 in dimethyl sulfoxide (DMSO) [34]) resulted in a peak $i_{cat}/i_p = 30$ (7.6 mA/cm$^2$ peak current density) and TOF = 2000 s$^{-1}$ at 3.2 M MeOH. The pronounced deviation of the catalytic CVs from a steady-state "S-shaped" wave (Figure 5.17b) with peak maximum at ~–2.2 V versus $Fc^+$/Fc and especially the peak in the return oxidation (~–2.1 V vs. $Fc^+$/Fc) is quite unusual, likely arising from multiple factors. The main factor contributing to this odd current response is an overlapping bpy-based reduction at ~–2.3 V versus $Fc^+$/Fc [30].

### 5.3.3 Calculation of Heterogeneous Rate Constant $\kappa^0$

The standard rate constant for the heterogeneous electron transfer between the electrode and the redox species can be determined for voltammetric data using the dimensionless rate parameter $\psi$ defined by Equation 5.15 [3]:

$$\psi = \frac{(D_O/D_k)^{\alpha/2}k^0}{(\pi D_O fv)^{1/2}} \tag{5.15}$$

$f$ is a constant defined by $f = F/RT$. $D_O/D_R$ is the ratio of the diffusion coefficient of the starting material ($D_O$) and the diffusion coefficient of the reduced species formed by the electron transfer ($D_R$) to the power of $\alpha/2$. When the $D_R$ value is not expected to change compared to that of $D_O$ giving $D_O/D_R = 1$. This means that the transfer coefficient term, $\alpha$, does not need to be considered and the equation can be simplified to give Equation 5.16:

$$\psi = \frac{k^0}{(\pi D_O fv)^{1/2}} \tag{5.16}$$

By comparison of this with ideal data generated from numerical simulation of the electrochemical problem, $k^0$ can be determined for experimental data [3].

### 5.3.4 Homogeneous Electron-Transfer Rate Constant $\kappa'$

The homogeneous rate constant can be determined if the reaction mechanism is known. For the $E_rC_i'$ mechanism, the plot as shown in Figure 5.18 can be employed, along with voltammetric data to gather $\lambda^{1/2}$ values.

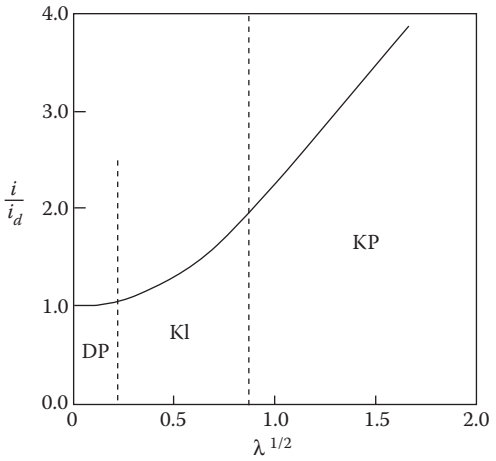


**FIGURE 5.18** Ratio of kinetic peak current for the $E_rC_i'$ reaction scheme to diffusion-controlled peak current as a function of $\lambda^{1/2}$. (Bard, A. J. and Faulkner, L. R.: *Electrochemical Methods*: *Fundamentals and Applications*. 2nd edn. p. 502. 2001. Copyright Wiley-VCH Verlag GmbH & Co. KGaA. Reproduced with permission.)

The kinetic parameter $\lambda$ is defined by Equation 5.17:

$$\lambda = \frac{k'C_Z^*}{v}\left(\frac{RT}{nF}\right) \tag{5.17}$$

where $C_Z^*$ is the bulk concentration of the species present in excess which undergoes electron transfer from the redox species, such as $[CO_2]$; so with the experimental scan rates employed, a value of $k'$ can be established. In Figure 5.18, the DP zone is where there is pure diffusion control of the peak current. The peak current here is proportional to the square root of the scan rate and is reversible. The KP region is purely kinetically controlled with no diffusion contribution; therefore the peak current is independent of the scan rate. Complete kinetic control would be expected to result in the voltammogram shifting from peak shaped toward a sigmoidal form with a steady-state current being reached [3,35]. The KI region is the transitional region where both diffusion and kinetics play a part in the control of the limiting current and therefore the current ratio.

CV is not always particularly well suited for quantitative analysis of a system although it is easily employed for qualitative studies and the evaluation of potentials associated with electron transfer, etc.

## 5.4 ROTATING DISK ELECTRODE AND ROTATING RING-DISK ELECTRODE TECHNIQUES

### 5.4.1 Rotating Disk Electrode Technique

The rotating disk electrode (RDE) is a hydrodynamic technique where diffusion limitation plays a vital role, and forced convection is the dominant form of mass

transport. Convection, which implies movement of the solution with respect to the electrode surface, is a much more effective form of transport than diffusion and when controlled allows for excellent reproducibility and increased sensitivity in electrochemical measurements. The RDE consists of a standard macroelectrode encased in insulating material that can be set to rotate about its own axis at selected specific frequencies, $f$ (revolutions per second), which can be easily transformed to angular velocity, ω, through Equation 5.18:

$$\omega = 2\pi f \tag{5.18}$$

The convective flow of electrolyte to the electrode surface produced by the rotation is shown in the schematic Figure 5.19.

Rather than the diffusion-related peaks seen in CV, RDE gives a steady-state limiting current response dependent upon the fixed angular velocity employed as illustrated in the Levich equation [3] for the RDE (5.19):

$$I_l = 0.62nFAD^{2/3}v^{-1/6}C\omega^{1/2} \tag{5.19}$$

where ν is the kinematic viscosity of the electrolyte solution. The presence of the diffusion coefficient, $D$, in the equation describing a convection-controlled system may seem contradictory; however, although convection is dominant in the bulk solution, there is still a thin layer close to the electrode surface where diffusion plays an important role. The thickness of this layer (δ) is dependent on rotational velocity as shown by Equation 5.20 [19]:

$$\delta = \frac{1.61D^{1/3}v^{1/6}}{\omega^{1/2}} \tag{5.20}$$

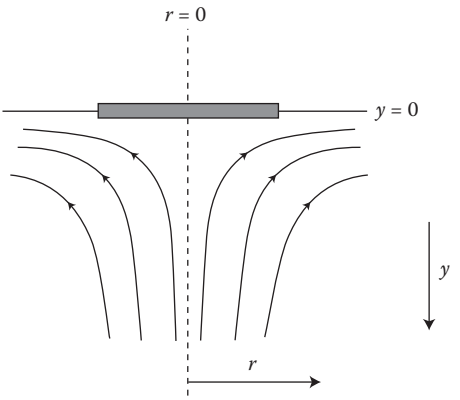


**FIGURE 5.19** Schematic depicting RDE convective flow. (Bard, A. J. and Faulkner, L. R.: *Electrochemical Methods*: *Fundamentals and Applications*. 2nd edn. p. 337. 2001. Copyright Wiley-VCH Verlag GmbH & Co. KGaA. Reproduced with permission.)

### 5.4.2 Rotating Ring-Disk Electrode Technique

Generating a product or an intermediate at a disk electrode and collecting it at a ring electrode that concentrically surrounds the disk is an alternative to CV. The product or intermediate is generated by fixing the disk potential at an appropriate value and scanning the ring potential so as to obtain its oxidative or reductive signature as a steady-state current–potential curve. This technique has been extensively and successfully applied in the determination of the product, for example, CO, in the catalytic reduction of $CO_2$.

### 5.4.3 Practical Application for $CO_2$ Electroreduction

The electrocatalytic activity of the complex *N*,*N*′,*N*″,*N*′-tetramethyltetra-3,4-pyridoporphyrazinocobalt(II) ([Co(II)(Tmtppa)]$^{4+}$, Co(Tmtppa)) toward $CO_2$ reduction, is investigated using a rotating ring (platinum)-disk(EPG|Co(Tmtppa)|Nafion® electrode, consisting of an edged pyrolytic graphite (EPG) disk, modified with Co(Tmtppa) fixed by a Nafion film, and a polycrystalline platinum ring as shown in Figure 5.20 [36]. In a supporting electrolyte solution (0.1 M $NaClO_4$ + 0.1 M $CH_3COOH + H_3BO_3 + H_3PO_4$ + NaOH buffer, pH 5.5) containing dissolved $CO_2$, when the rotating Co(Tmtppa)-modified EPG disk electrode is poised at a potential desirable for the electrocatalytic reduction of $CO_2$, the *in situ* formed product of CO will be thrown on to the platinum ring electrode and can be identified and detected with CV. As observed, a spark-like oxidation peak near 0.4 V appears in Figure 5.20b–d, indicating a surface process arising from the adsorbed CO, whereas hydrogen adsorption–desorption currents in the potential range 0 to −0.5 V gradually disappear, indicative of the strong competitive adsorption of CO at the hydrogen adsorption sites. A linear relationship between the ring current due to CO oxidation and $CO_2$ concentration in aqueous solution at certain range is observed as shown in Figure 5.20e, further confirming that the source of CO was in fact the $CO_2$ electrocatalytic reduction by immobilized Co(Tmtppa). When the dissolved $CO_2$ concentration exceeds $8 \times 10^{-3}$ M, the current reaches a plateau, probably due to the saturated adsorption on the ring electrode by the CO produced at the disk electrode. The CO oxidation reaction on the Pt ring electrode can be assigned to

$$[CO]_{ads} + H_2O \rightarrow CO_2 + 2H^+ + 2e^- \tag{5.21}$$

whereas the following shoulder near 0.5 V is recognized as splitting of the oxidation peak due to the effects of anion adsorption [37].

To ascertain the effect of mass transport limitations on the electrocatalytic reduction of $CO_2$ in 18 mol% EMIM-$BF_4$, electrochemical experiments using a rotating disk electrode (RDE) of Ag NPs-modified Au RDE polarized to −1.6 V versus AgQRE at the rotation speed range of 500–5000 rpm are carried out. As shown in Figure 5.21, in the absence of most mass transport effects, the turnover rate of the chemical reaction of interest can reach up to 60 turnovers per second and 62.1 mA/cm$^2$, based on the steady-state current measurements as a function of rotation speed [14].

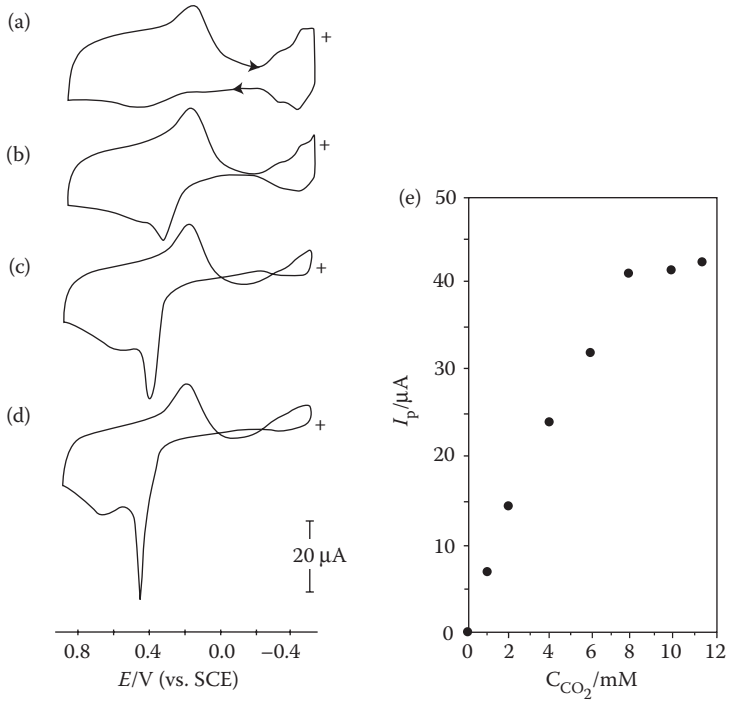


**FIGURE 5.20** Ring electrode cyclic voltammograms of a rotating ring (platinum)-disk (EPG|Co(Tmtppa)|Nafion) electrode, recorded at a disk potential of −1.1 V in a supporting electrolyte solution (0.1 M $NaClO_4$ + 0.1 M $CH_3COOH$ + $H_3BO_3$ + $H_3PO_4$ + NaOH buffer, pH 5.5) containing various concentrations of $CO_2$: (a) 0; (b) $2.0 \times 10^{-3}$ M; (c) $5.9 \times 10^{-3}$ M; and (d) $1.13 \times 10^{-2}$ M. Ring potential scan rate: 100 mV/s. Rotation rate: 900 rpm. (e) Ring CO oxidation peak currents near 0.4 V as a function of $CO_2$ concentration. (Reprinted from *Journal of Electroanalytical Chemistry,* 403(1–2), Zhang, J., Pietro, W. J. and Lever, A. B. P., Rotating ring-disk electrode analysis of $CO_2$ reduction electrocatalyzed by a cobalt tetramethylpyridoporphyrazine on the disk and detected as CO on a platinum ring, 93–100, Copyright 1996, with permission from Elsevier.)

## 5.5 ELECTROCHEMICAL IMPEDANCE SPECTROSCOPY

### 5.5.1 Basic Concept

Electrochemical impedance spectroscopy is a linear nondestructive technique, with high precision and a wide time span of $10^4$–$10^{-6}$ s or large frequency range of $10^{-4}$–$10^6$ Hz, due to the application of small perturbations to a system at equilibrium, which is powerful for the mechanism investigation of electrode reactions, the measurement of the dielectric and transport properties of materials, and the exploration of the properties of porous electrodes [3,38–41].

Generally, an electrode/electrolyte interface is considered simply an impedance to a small sinusoidal excitation and is described theoretically in terms of an EEC.

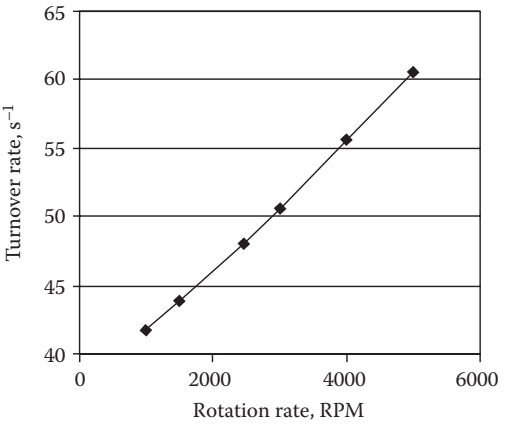


**FIGURE 5.21** Turnover rate measured with a RDE at −0.9 V vs. normal hydrogen electrode (NHE) for $CO_2$ reduction on Ag NPs in 18 mol% EMIM-$BF_4$. (Reproduced from Rosen, B. A. et al. *Science*, 2011; 334(6056): 643–644. With permission from Science.)

By the electrical analogs, the electrochemical data are explained. For a fast charge-transfer reaction at a planar electrode,

$$O + ne \underset{k_b}{\overset{k_f}{\rightleftharpoons}} R \tag{5.22}$$

with both the oxidant $O$ and the reductant $R$ soluble, the electrified interface, illustrated in Figure 5.22a first proposed by Helmholtz [42], can be modeled by the Randles equivalent circuit [43] as shown in Figure 5.22b, which provides the most effective simulation of the impedance characteristics of the fast reaction. As observed in Figure 5.22, each component at the interface and in the solution during an electrochemical reaction is represented by comparison with a physical component. A double-layer capacitor, $C_d$, is in parallel with a pure polarization resistor, $R_p$, and a Warburg impedance, $Z_w$, then connected in series with a solution resistor, $R_s$. Among them, $R_p$ is a function of potential and becomes the charge-transfer resistance, $R_{ct}$, at $\eta = 0$, which manifests the kinetics of heterogeneous charge transfer. Warburg impedance has no simple electrical analog, related to diffusional mass transfer. The faradaic impedance, $Z_f$, broken down into two components of $R_p$ and the Warburg impedance, represents the effect of the heterogeneous electron-transfer process. The equivalent circuit is dependent on the type of a real electrochemical reaction involved at the interface, which could be much more complicated than the frequently used Randles circuit mentioned above. Here, the simplest electrode process, involving no adsorption of electroreactants, no multistep charge transfer, or no homogeneous chemistry, is discussed as in Figure 5.22. The positive charged oxidants accept electrons from the electrode at the interface and diffuse in, whereas the generated reductants flow out into the bulk of the solution.

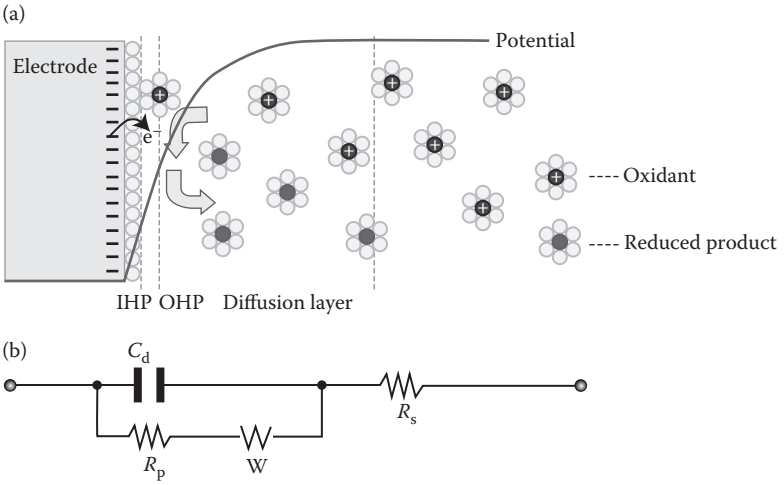


**FIGURE 5.22** Simple electrified interface with no specific adsorption, in which the vertical dotted lines in (a) are represented by the electronic components in (b). (a) IHP and OHP are the inner and outer Helmholtz planes, respectively. (Reprinted with permission from Park, S.-M. and Yoo, J.-S. Peer reviewed: Electrochemical impedance spectroscopy for better electrochemical measurements. *Analytical Chemistry*. 75(21), 455 A–461 A. Copyright 2003 American Chemical Society.)

The total impedance of an interface, $Z(\omega)$, is frequency-dependent and consists of two parts, a real number $Z'(\omega)$ and an imaginary number $Z''(\omega)$, expressed by $Z(\omega) = Z'(\omega) + jZ''(\omega)$ with the phase angle of $\phi = \tan^{-1}\,[Z''(\omega)/Z'(\omega)]$. Chemical information, such as system characteristics, $R_s$, $R_p$, and $C_d$ for an electrochemical reaction, can be extracted by treating the impedance data over Nyquist complex plane plots, in which $Z''(\omega)$ is plotted against $Z'(\omega)$ for different $\omega$ ($\omega = 2\pi f$ with $f$ being the frequency).

For the reaction (5.22), described by the Butler–Volmer equation, with the circuit elements shown in Figure 5.22b at the interface, the derived impedance expression can be simplified by considering the limiting behavior at high and low frequency:

1. At very high frequency, the contribution of the Warburg component is negligible in relation to $R_p$; the impedance is [41]

$$Z(\omega) = R_s + \frac{R_p}{1 + j\omega R_p C_d} = R_s + \frac{R_p}{1 + \omega^2 R_p^2 C_d^2} - \frac{j\omega R_p^2 C_d}{1 + \omega^2 R_p^2 C_d^2} = Z' + Z'' \qquad (5.23)$$

2. At low frequency, the contribution of the Warburg component becomes important as the electron-transfer process at the interface may be limited by the mass transport of the electroactive species; the impedance is [41]

$$Z(\omega) = R_s + R_p\left[1 + \frac{\lambda}{\sqrt{2\omega}}\right] - R_p^2 \lambda_2 C_d - \frac{jR_p\lambda}{\sqrt{2\omega}} \qquad (5.24)$$

where in $\lambda = (k_f/\sqrt{D_O}) + (k_b/\sqrt{D_R})$, $k_f$ and $k_b$ are the forward and backward electron-transfer rate constants, respectively, as shown in Equation 5.22. And, the frequency-dependent term of $\lambda/\sqrt{2\omega}$, appearing in both the real and the imaginary parts in Equation 5.24 is called the Warburg impedance.

Figure 5.23 shows the Nyquist plots for an electrochemical system, based on computer-generated data using Equation 5.24 at arbitrarily picked values of $R_p$, whereas the contribution of the Warburg impedance in stars is only for $R_p = 2$ kΩ. As observed, the plot of $Z''(\omega)$ versus $Z'(\omega)$ is linear and has unit slope with the phase angle approaching 45° when the Warburg contribution becomes dominant in the low-frequency regime, characteristic of a diffusion-controlled electrode process. The intercept of the dashed line, representing Warburg components, is at $R_s + R_p - R_p^2\lambda^2 C_d^2$ from which $\lambda = 38$ is obtained; therefore, $k_f = 4.1 \times 10^{-3}$ cm/s for a diffusion coefficient of $1.8 \times 10^{-6}$ cm²/s. $R_s$, 10 Ω; $C_d$, 20 μF; $R_p$ value from inside to outside at 100 Ω, 500 Ω, 1 kΩ, 2 kΩ, respectively. Otherwise, with the obtained value of λ and the calculated $k_f$ from $i_f = nFAk_fC_O$ ($C_O$, the bulk concentration of oxidant and $A$, the electrode area), the diffusion coefficient can be thereby calculated. According to Equation 5.23 as depicted in Figure 5.23, at high frequencies, $Z''(\omega)$ versus $Z'(\omega)$ gives a circular plot centered at $Z'(\omega) = R_s + R_p/2$ and $Z''(\omega) = 0$ and having a radius of $R_p/2$, where a maximum $Z''(\omega)$ is observed with the relationship of $R_p \times C_d = 1/\omega_{max} = 1/2\pi f_{max} = \tau_{rnx}$. Here, $\tau_{rnx}$ is the time constant of the electrochemical reaction, indicating how fast the reaction takes place. Also, from $R_p \times C_d$, $C_d$ can be obtained as $R_p$ is already known from the intercept on the $Z'(\omega)$ axis [41].

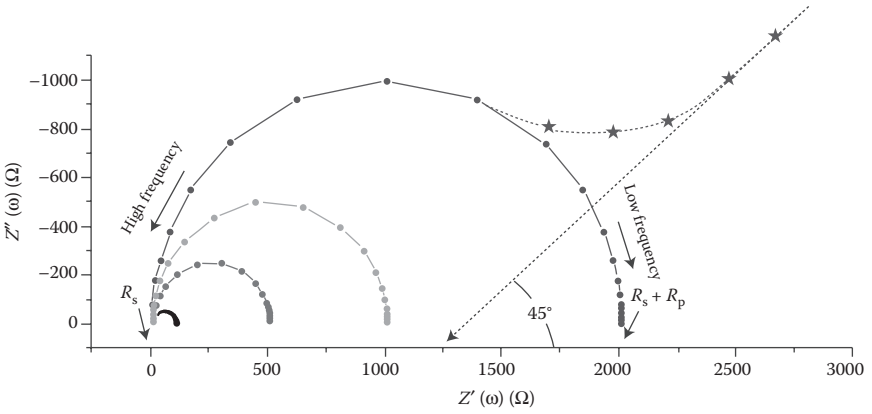


**FIGURE 5.23** Nyquist plots for an electrochemical system. Regions of mass transfer and kinetic control are found at low and high frequencies, respectively. (Reprinted with permission from Park, S.-M. and Yoo, J.-S. Peer Reviewed: Electrochemical impedance spectroscopy for better electrochemical measurements. *Analytical Chemistry*. 75(21), 455 A–461 A. Copyright 2003 American Chemical Society.)

### 5.5.2 Practical Application for $CO_2$ Electroreduction

Electrochemical impedance spectroscopy was carried out to investigate the cell or electrode process for the electrochemical reduction of $CO_2$.

The electroreduction of $CO_2$ into CO and $CH_4$ in a proton conducting solid oxide electrolyzer with iron/iron oxide composite cathode using $BaCe_{0.5}Zr_{0.3}Y_{0.16}Zn_{0.04}O_{3-\delta}$ (BCZYZ) as an electrolyte was investigated by *in situ* AC impedance spectroscopy as shown in Figure 5.24 [44]. The $R_s$ is mainly from the BCZYZ electrolyte, which keeps almost constant and decreases slightly with increasing voltage, indicating increased electronic conduction as well as some oxygen-ion conduction at higher potentials. The $R_p$ is from electrode polarization, which displays sharp increases from 5.1 to 11.2 $\Omega$ cm$^2$ at low voltage from 0 to 0.5 V, decreases from 6.3 to 0.4 $\Omega$ cm$^2$ at high voltage from 1.0 to 2.0 V, and remains stable above 2.0 V, indicating activation of the redox processes dominate early stages at low voltage, whereas desirable electrode reactions with favorable thermodynamics and kinetics result in a large drop in $R_p$ at high voltage. The adsorption and diffusion processes on the electrode at low frequency below 10 kHz might be the rate-limiting step of the electrode process. The summit frequency of the process at low frequency changes from 0.5 to 19.9 Hz when the external load increases from 0.5 to 2.0 V, demonstrating an improvement of the low-frequency process at higher external loads.

## 5.6 CHRONOAMPEROMETRY

### 5.6.1 Basic Concept

CA involves the application of a fixed potential at a stationary electrode in an unstirred solution with the working electrode area kept small compared to the volume of solution under investigation. The current produced is measured as a function of time to give current transients or chronoamperograms. CA, like CV, usually involves an initial potential at which no reaction is anticipated therefore minimal current flows, $E_i$, which is then stepped to a set potential where the electron transfer of interest (either oxidation or reduction) takes place, $E_s$. The potential scheme is given in Figure 5.25.

The concentration of the substrate at the electrode surface during the application of $E_s$ is constantly approaching zero as it reacts to form a new species, creating a diffusion layer or depletion zone, and as such a concentration gradient to produce diffusion of the substrate from the bulk solution to the electrode surface and of the new species accumulating at the electrode toward the bulk phase. The diffusion layer increases with time as the electroactive substrate is depleted, resulting in lowering current responses [19]. The diffuse layer is the region over which the potential varies. This, as well as the electrical double layer, found in the solution immediately adjacent to the electrode, is depicted in Figure 5.26.

Figure 5.26 shows the potential change between the electrode surface ($\Phi^M$) and the bulk solution ($\Phi^S$) with distance from the electrode. Upon moving from the electrode surface, the first layer reached is the inner Helmholtz plane (IHP), which is defined as the locus of the electrical centers of the specifically adsorbed ions on the electrode surface. This specific adsorption is not necessarily charge dependent and

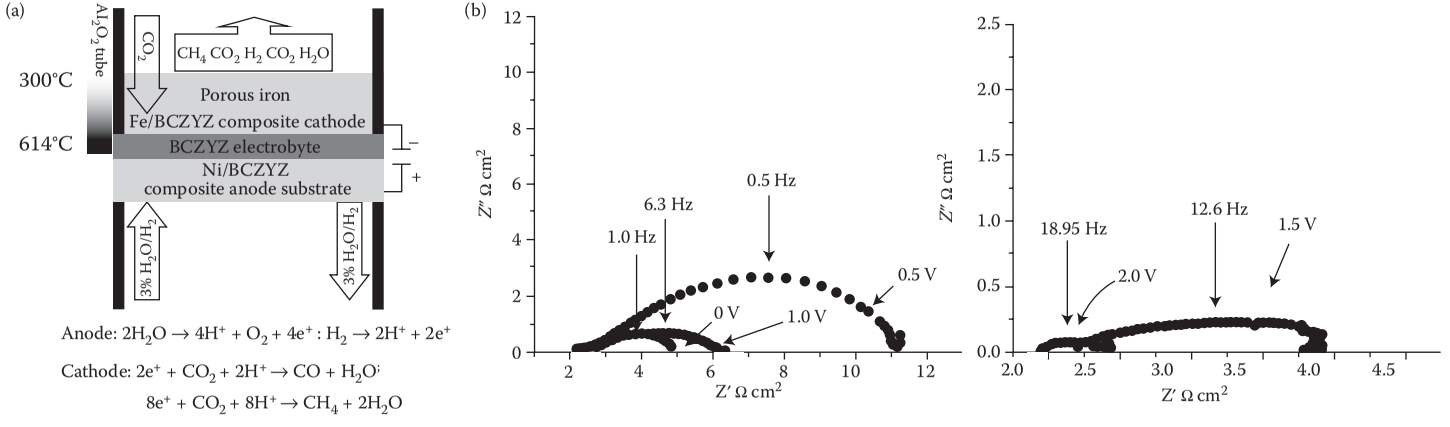


**FIGURE 5.24** (a) Schematic testing conditions of solid oxide electrolyzer. (b) AC impedance of solid oxide electrolyzer with different potentials. (Xie, K. et al. Electrochemical reduction of $CO_2$ in a proton conducting solid oxide electrolyser. *Journal of Materials Chemistry*. 2011; 21(1): 195–198. Reproduced by permission of The Royal Society of Chemistry.)

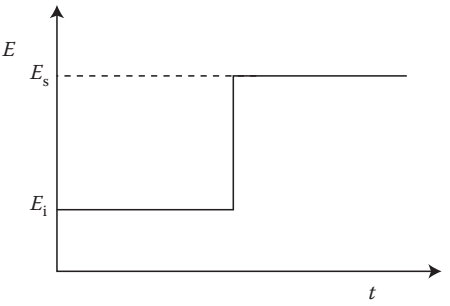


**FIGURE 5.25** Potential scheme for CA. (Bard, A. J. and Faulkner, L. R.: *Electrochemical Methods: Fundamentals and Applications*. 2nd edn. p. 157. 2001. Copyright Wiley-VCH Verlag GmbH & Co. KGaA. Reproduced with permission.)

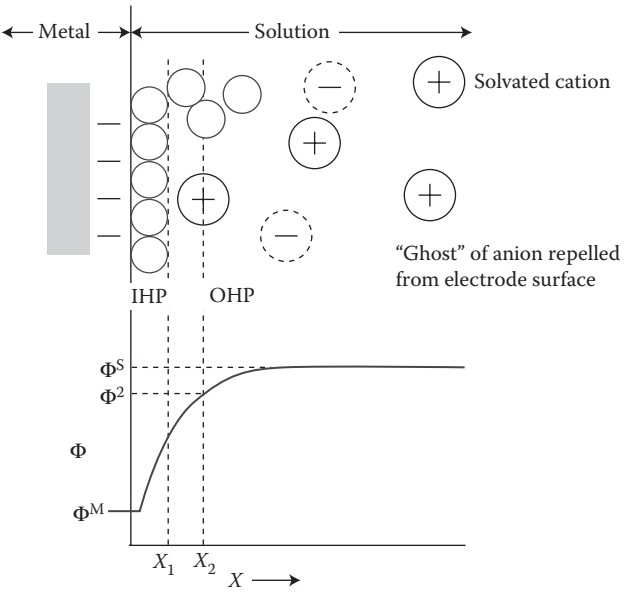


**FIGURE 5.26** Phase boundary at the electrode–electrolyte interface showing the electrical double layer and diffuse layer. (Bard, A. J. and Faulkner, L. R.: *Electrochemical Methods: Fundamentals and Applications*. 2nd edn. p. 14. 2001. Copyright Wiley-VCH Verlag GmbH & Co. KGaA. Reproduced with permission.)

consists of nonsolvated species. The next layer is the outer Helmholtz plane (OHP), which marks the minimum distance of these nearest solvated ions. The ions here are predominantly of the opposite charge to that of the electrode and are responsible for the sharp drop in potential as the charge difference between the electrode and bulk solution is balanced. These two layers make up what is termed the double layer. Beyond this point, the potential drop is more gradual as the concentration of excess

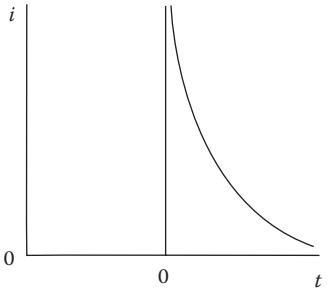


**FIGURE 5.27** Representative chronoamperogram of current flow versus time. (Bard, A. J. and Faulkner, L. R.: *Electrochemical Methods: Fundamentals and Applications.* 2nd edn. p. 157. 2001. Copyright Wiley-VCH Verlag GmbH & Co. KGaA. Reproduced with permission.)

counter ions decreases until the potential of bulk solution is matched marking the end of the diffuse layer [3].

A typical current transient can be seen in Figure 5.27.

At very short times, very high currents are usually produced due to the charging of the double layer (depicted in Figure 5.27). After this, the current drops as electrolysis occurs. The shape of the current transients is a result of the concentration gradients and Faraday's law (Equation 5.25) [45]:

$$Q = nFN \tag{5.25}$$

where the charge transferred, $Q$, corresponding to the integral of the current transient, is proportional to the number of electrons transferred per molecule $n$, and the moles of reactant $N$. The current observed is proportional to the flux of the electroactive species ($J$) using Fick's diffusion laws, as can be seen from Equation 5.26:

$$I = nFAJ = nFAD\left(\frac{\partial C(x)}{\partial x}\right)_{x=0} \tag{5.26}$$

At a planar electrode of working area, the Cottrell Equation 5.27 describes the instantaneous current [3]:

$$I = \frac{nFCD^{1/2}}{(\pi t)^{1/2}} \tag{5.27}$$

where the symbols are defined as previously with the addition of $t$ which is time. This relationship allows reproducible quantitative evaluation of the currents and diffusion coefficient of a system at high overpotentials where the diffusion to the electrode is the limiting mode of mass transport. At very short times, deviation due to the charging and instrumental error is anticipated and over prolonged application of potential (>10–20 s) convection may become significant; however, Cottrell plots,

where current is plotted as a function of $t^{-1/2}$, clearly show the period where the diffusion control is limiting with a linear region [3].

### 5.6.2 Practical Application for $CO_2$ Electroreduction

By CA, electrolytic $CO_2$ reduction at a nanoporous silver (np-Ag) electrode in a $CO_2$-saturated 0.5 M $KHCO_3$ was investigated as shown in Figure 5.28 [46]. At −0.60 V with an overpotential of 490 mV relative to the $CO_2$/CO equilibrium potential at −0.11 V versus reversible hydrogen electrode (RHE), a long-term stable current at ~18 mA/cm$^2$ throughout the electrocatalytic process was obtained with FE for CO calculated at ~92% (Figure 5.28a). The observed high initial current was thought from the reduction of a thin surface oxide layer formed in atmospheric air at about 0.5 nm thickness. By contrast, polycrystalline Ag displays a much lower current density of 0.47 mA/cm$^2$ and a poorer FE for CO at ~1.1% (Figure 5.28a) at the same condition. In addition, at more positive potential of −0.50 V with a lower overpotential of 390 mV, a smaller stable current of ~9.0 mA/cm$^2$ at an np-Ag electrode was observed with a CO efficiency decreased to ~90% (Figure 5.28b), whereas when the potential further positively increased to −0.40 V at 290 mV overpotential, the current dropped

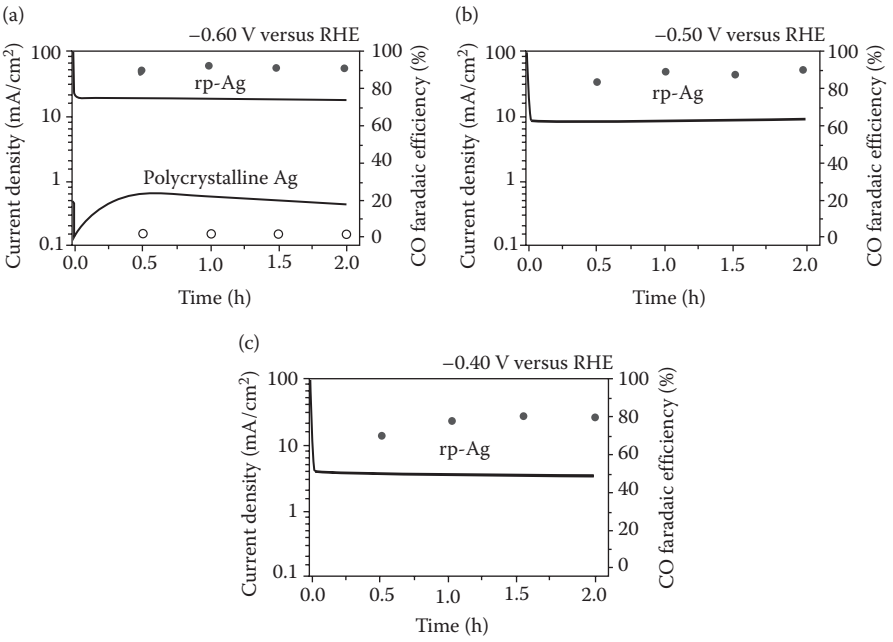


**FIGURE 5.28** $CO_2$ reduction activity of np-Ag and polycrystalline silver at (a) −0.60 V, np-Ag at (b) −0.50 V, and (c) −0.40 V versus RHE. Total current density versus time on (left axis) and CO FE versus time (right axis). (Reprinted by permission from Macmillan Publishers Ltd. *Nature Communications*. Lu, Q. et al. A selective and efficient electrocatalyst for carbon dioxide reduction. 5: 3242, copyright 2014.)

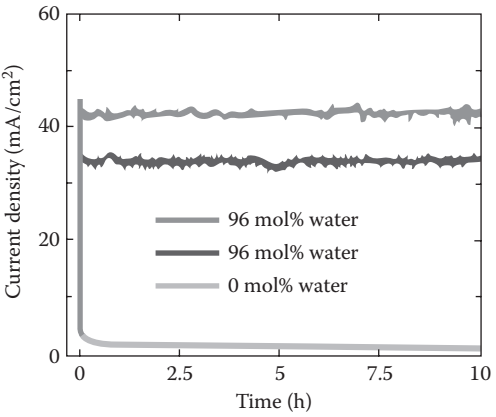


**FIGURE 5.29** Chronoamperometric curves of the bulk $MoS_2$ catalyst in $CO_2$-saturated EMIM-$BF_4$ solutions containing 96, 90, and 0 mol% water. (Reprinted by permission from Macmillan Publishers Ltd. *Nature Communications*. Asadi, M. et al. Robust carbon dioxide reduction on molybdenum disulphide edges. 5: 4470, copyright 2014.)

to ~3.3 mA/cm$^2$ with a CO efficiency only at ~79% (Figure 5.28c). Meanwhile, the rate of hydrogen evolution, occurred at a relatively small overpotential, increased correspondingly with the decrease of CO efficiency. The applied overpotential is not high enough to drive $CO_2$ reduction at a competitive rate [46].

The stability of the bulk $MoS_2$ catalyst for electrocatalytical reduction of $CO_2$ to CO is investigated at a prolonged period of 10 h in $CO_2$-saturated EMIM-$BF_4$ solutions containing 96, 90, and 0 mol% water by CA as shown in Figure 5.29 [13]. Stable steady-state current densities with negligible loss even after 10 h in all studied electrolytes are observed, indicating long-term stability and high efficiency of the $MoS_2$ catalyst. The more the water in the electrolyte, the higher the stable steady-state current densities, suggesting that water is involved in the $CO_2$ reduction reaction. The current density decreases rapidly at the initial period, attributed to the mass transport limitation from the bulk to the electrode surface without stirring. When the reaction rate of $CO_2$ electroreduction is governed by the reactant diffusion [3,24] after the reactant adjacent to the electrode surface is consumed immediately, a "steady-state current density" is observed. The obtained steady-state current density is much lower than that recorded in CV experiments at the same condition as there is an extra current due to interface charging involved in CV mode, but not for CA experiments [3,24].

### 5.6.3 Chronoamperometric $k'$ Determination

In a similar manner to the voltammetric $k'$ determination, the homogeneous rate constant can be evaluated using chronoamperometric data and the working curve reproduced in Figure 5.30.

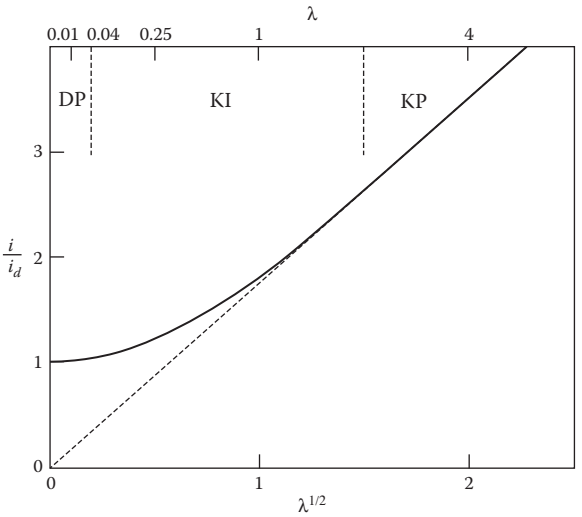


**FIGURE 5.30** Chronoamperometric working curve for the $E_rC_i'$ case for various values of $\lambda^{1/2}$. (Bard, A. J. and Faulkner, L. R.: *Electrochemical Methods: Fundamentals and Applications*. 2nd edn. p. 504. 2001. Copyright Wiley-VCH Verlag GmbH & Co. KGaA. Reproduced with permission.)

The λ values are related to $k'$ for chronoamperometric experiments through Equation 5.28:

$$\lambda = K'C_z^* t \tag{5.28}$$

The plot is again split into the three zones described above for voltammetry but with the dashed line from the origin showing the KP region limiting line.

## 5.7 CHRONOPOTENTIOMETRY

Opposite to CA, for chronopotentiometry, the experiment is carried out by applying a constant current between stationary working and auxiliary electrodes with a galvanostat and recording the potential between the working and reference electrodes as the dependent variable as a function of time to give potential transients or chronopotentiograms, at similar condition such as small ratio of electrode area to solution volume and semi-infinite diffusion. The obvious disadvantage of controlled-current techniques is that double-layer charging effects occur throughout the experiment with larger values and no straightforward correction is available, though they can be of particular value for background process studying. Constant-current chronopotentiometry involves a set current $i$, where the electron transfer of interest (either oxidation or reduction) takes place at a constant rate. The current scheme is given in Figure 5.31a.

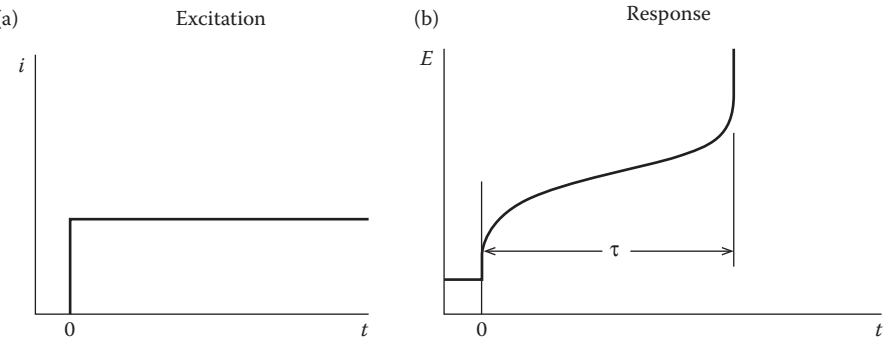


**FIGURE 5.31** (a) Current scheme as a function of time for chronopotentiometry. (b) A representative chronopotentiogram of potential change versus time. (Bard, A. J. and Faulkner, L. R.: *Electrochemical Methods: Fundamentals and Applications*. 2nd edn. p. 307. 2001. Copyright Wiley-VCH Verlag GmbH & Co. KGaA. Reproduced with permission.)

A typical potential transient can be seen in Figure 5.31b. When the steady current is applied, the electrode potential directly moves to values characteristic of the redox active couple. As the electrolysis continues, the potential varies since the concentration ratio of the oxidative/reductive species on the surface of the electrode changes with time. At the transition time, the concentration of active species drops to zero, then the flux of active species to the electrode surface is not large enough to accept or donate all electrons being forced across the electrode–solution interface, and the electrode potential rapidly shifts to a more extreme value where a new, second redox process can occurs. The shape and location of the resulting *E–t* curve are governed by the reversibility, or the heterogeneous rate constant, of the redox process. The transition time, $\tau$, is defined as the time span from the beginning of the application of the constant current to the sharp decrease or increase in the electrode potential, which is the chronopotentiometric analog of the peak or limiting current, and related to the concentration and the diffusion coefficient.

At a planar working electrode in an unstirred solution, the Sand equation (5.29) describes the transition time, $\tau$:

$$\frac{i\tau^{1/2}}{C^*} = \frac{nFAD^{1/2}\pi^{1/2}}{2} = 85.5nD^{1/2}A\frac{mA - s^{1/2}}{mM} (\text{with } A \text{ in cm}^2) \tag{5.29}$$

where the symbols either have their usual meanings or are defined as above. The $i\tau^{1/2}/c^*$ is called transition time constant, which is independent of $i$ or $c$ for a well-behaved system. The measured value of $\tau$ at known $i$ or $i\tau^{1/2}$ values at various currents can be used to determine $n$, $A$, $c$, or $D$. A lack of constancy in the parameter of $i\tau^{1/2}/c^*$ reflects a complicated electrode process, probably involving in a coupled homogeneous chemical reaction or adsorption, or due to double-layer charging or the onset of convection.

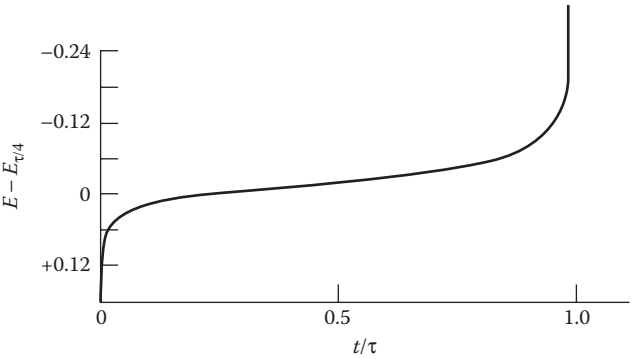


**FIGURE 5.32** Theoretical chronopotentiogram for a Nernstian electrode process. (Bard, A. J. and Faulkner, L. R.: *Electrochemical Methods: Fundamentals and Applications.* 2nd edn. p. 310. 2001. Copyright Wiley-VCH Verlag GmbH & Co. KGaA. Reproduced with permission.)

For a Nernstian wave with rapid electron transfer, a convenient diagnostic between the electrode potential, $E$ and the quarter-wave potential of $E_{\tau/4}$ which is the chronopotentiometric equivalent of the voltammetric $E_{1/2}$, is expressed by Equation 5.30:

$$E = E_{\tau/4} + \frac{RT}{nF} \ln \frac{\tau^{1/2} - t^{1/2}}{t^{1/2}} \tag{5.30}$$

where $E_{\tau/4}$ is

$$E_{\tau/4} = E^{0'} - \frac{RT}{2nF} \ln \frac{D_O}{D_R} \tag{5.31}$$

For a reversible electrode process, the $E$–$t$ curve is a linear plot of $E$ versus log $(\tau^{1/2} - \tau^{1/2})/\tau^{1/2}$ with a slope of $59/n$ mV at 25°C. The theoretical chronopotentiogram for a Nernstian electrode process is shown in Figure 5.32.

## REFERENCES

1. Jitaru, M., Lowy, D. A., Toma, M., Toma, B. C. and Oniciu, L. Electrochemical reduction of carbon dioxide on flat metallic cathodes. *Journal of Applied Electrochemistry.* 1997; 27(8): 875–889.
2. Hossain, S. *Electrochemical Reduction of Carbon Dioxide to Hydrocarbons.* King Fahd University of Petroleum and Minerals, Saudi Arabia. 2011.
3. Bard, A. J. and Faulkner, L. R. *Electrochemical Methods: Fundamentals and Applications.* 2nd edn. New York, NY: John Wiley & Sons, Inc. 2001.
4. Delacourt, C., Ridgway, P. L. and Newman, J. Mathematical modeling of $CO_2$ reduction to CO in aqueous electrolytes: I. Kinetic study on planar silver and gold electrodes. *Journal of the Electrochemical Society.* 2010; 157(12): B1902–B1910.

5. Medina-Ramos, J., DiMeglio, J. L. and Rosenthal, J. Efficient reduction of $CO_2$ to CO with high current density using *in situ* or *ex situ* prepared bi-based materials. *Journal of the American Chemical Society*. 2014; 136(23): 8361–8367.
6. Russell, P., Kovac, N., Srinivasan, S. and Steinberg, M. The electrochemical reduction of carbon dioxide, formic acid, and formaldehyde. *Journal of the Electrochemical Society*. 1977; 124(9): 1329–1338.
7. Paik, W., Andersen, T. N. and Eyring, H. Kinetic studies of the electrolytic reduction of carbon dioxide on the mercury electrode. *Electrochimica Acta*. 1969; 14(12): 1217–1232.
8. Haynes, L. V. and Sawyer, D. T. Electrochemistry of carbon dioxide in dimethyl sulfoxide at gold and mercury electrodes. *Analytical Chemistry*. 1967; 39(3): 332–338.
9. Ryu, J., Andersen, T. N. and Eyring, H. Electrode reduction kinetics of carbon dioxide in aqueous solution. *The Journal of Physical Chemistry*. 1972; 76(22): 3278–3286.
10. Spataru, N., Tokuhiro, K., Terashima, C., Rao, T. and Fujishima, A. Electrochemical reduction of carbon dioxide at ruthenium dioxide deposited on boron-doped diamond. *Journal of Applied Electrochemistry*. 2003; 33(12): 1205–1210.
11. Medina-Ramos, J., Pupillo, R. C., Keane, T. P., DiMeglio, J. L. and Rosenthal, J. Efficient conversion of $CO_2$ to CO using tin and other inexpensive and easily prepared post-transition metal catalysts. *Journal of the American Chemical Society*. 2015; 137(15): 5021–5027.
12. Zhang, S., Kang, P. and Meyer, T. J. Nanostructured tin catalysts for selective electrochemical reduction of carbon dioxide to formate. *Journal of the American Chemical Society*. 2014; 136(5): 1734–1737.
13. Asadi, M., Kumar, B., Behranginia, A., Rosen, B. A., Baskin, A., Repnin, N., Pisasale, D. et al. Robust carbon dioxide reduction on molybdenum disulphide edges. *Nature Communications*. 2014; 5: 4470.
14. Rosen, B. A., Salehi-Khojin, A., Thorson, M. R., Zhu, W., Whipple, D. T., Kenis, P. J. A. and Masel, R. I. Ionic liquid–mediated selective conversion of $CO_2$ to CO at low overpotentials. *Science*. 2011; 334(6056): 643–644.
15. Chen, Y., Li, C. W. and Kanan, M. W. Aqueous $CO_2$ reduction at very low overpotential on oxide-derived au nanoparticles. *Journal of the American Chemical Society*. 2012; 134(49): 19969–19972.
16. Salehi-Khojin, A., Jhong, H.-R. M., Rosen, B. A., Zhu, W., Ma, S., Kenis, P. J. A. and Masel, R. I. Nanoparticle silver catalysts that show enhanced activity for carbon dioxide electrolysis. *The Journal of Physical Chemistry C*. 2013; 117(4): 1627–1632.
17. Rosen, B. A., Haan, J. L., Mukherjee, P., Braunschweig, B., Zhu, W., Salehi-Khojin, A., Dlott, D. D. and Masel, R. I. *In situ* spectroscopic examination of a low overpotential pathway for carbon dioxide conversion to carbon monoxide. *The Journal of Physical Chemistry C*. 2012; 116(29): 15307–15312.
18. Kissinger, P. T. and Heineman, W. R. *Laboratory Techniques in Electroanalytical Chemistry, Revised and Expanded*. 2nd edn. New York: Marcel Dekker Inc. 1996.
19. Fischer, A. *Electrode Dynamics*. Oxford: Oxford University Press. 1996.
20. Girault, H. H. *Analytical and Physical Electrochemistry*. New York: Marcel Dekker, Inc. 2004.
21. Shironita, S., Karasuda, K., Sato, M. and Umeda, M. Feasibility investigation of methanol generation by $CO_2$ reduction using Pt/C-based membrane electrode assembly for a reversible fuel cell. *Journal of Power Sources*. 2013; 228(0): 68–74.
22. Conway, B. E., Angerstein-Kozlowska, H., Sharp, W. B. A. and Criddle, E. E. Ultrapurification of water for electrochemical and surface chemical work by catalytic pyrodistillation. *Analytical Chemistry*. 1973; 45(8): 1331–1336.
23. Guo, X., Zhang, Y., Deng, C., Li, X., Xue, Y., Yan, Y.-M. and Sun, K. Composition dependent activity of Cu–Pt nanocrystals for electrochemical reduction of $CO_2$. *Chemical Communications*. 2015; 51(7): 1345–1348.

24. Kumar, B., Asadi, M., Pisasale, D., Sinha-Ray, S., Rosen, B. A., Haasch, R., Abiade, J., Yarin, A. L. and Salehi-Khojin, A. Renewable and metal-free carbon nanofibre catalysts for carbon dioxide reduction. *Nature Communications*. 2013; 4: 2819.
25. Rosen, B. A., Zhu, W., Kaul, G., Salehi-Khojin, A. and Masel, R. I. Water enhancement of $CO_2$ conversion on silver in 1-ethyl-3-methylimidazolium tetrafluoroborate. *Journal of the Electrochemical Society*. 2013; 160(2): H138–H141.
26. Froehlich, J. D. and Kubiak, C. P. The homogeneous reduction of $CO_2$ by [Ni(cyclam)]+: Increased catalytic rates with the addition of a CO scavenger. *Journal of the American Chemical Society*. 2015; 137(10): 3565–3573.
27. Zilbermann, I., Winnik, M., Sagiv, D., Rotman, A., Cohen, H. and Meyerstein, D. Properties of monovalent nickel complexes with tetraaza-macrocyclic ligands in aqueous solutions. *Inorganica Chimica Acta*. 1995; 240(1–2): 503–514.
28. Gagne, R. R., Allison, J. L. and Ingle, D. M. Unusual structural and reactivity types for copper(I). Equilibrium constants for the binding of monodentate ligands to several four-coordinate copper(I) complexes. *Inorganic Chemistry*. 1979; 18(10): 2767–2774.
29. Beley, M., Collin, J. P., Ruppert, R. and Sauvage, J. P. Electrocatalytic reduction of carbon dioxide by nickel cyclam2+ in water: Study of the factors affecting the efficiency and the selectivity of the process. *Journal of the American Chemical Society*. 1986; 108(24): 7461–7467.
30. Sampson, M. D., Nguyen, A. D., Grice, K. A., Moore, C. E., Rheingold, A. L. and Kubiak, C. P. Manganese catalysts with bulky bipyridine ligands for the electrocatalytic reduction of carbon dioxide: Eliminating dimerization and altering catalysis. *Journal of the American Chemical Society*. 2014; 136(14): 5460–5471.
31. Tulyathan, B. and Geiger, W. E. Structural consequences of electron-transfer reactions. Part 12. Multi electron processes involving structural changes. The two-electron reduction of hexaosmium carbonyl cluster (Os6(CO)18). *Journal of the American Chemical Society*. 1985; 107(21): 5960–5967.
32. Savéant, J. M. and Vianello, E. Potential-sweep chronoamperometry theory of kinetic currents in the case of a first order chemical reaction preceding the electron-transfer process. *Electrochimica Acta*. 1963; 8(12): 905–923.
33. Bard, A. J. and Faulkner, L. R. *Electrochemical Methods*. New York: Wiley, 1980.
34. Olmstead, W. N., Margolin, Z. and Bordwell, F. G. Acidities of water and simple alcohols in dimethyl sulfoxide solution. *The Journal of Organic Chemistry*. 1980; 45(16): 3295–3299.
35. Costentin, C., Robert, M. and Saveant, J.-M. Catalysis of the electrochemical reduction of carbon dioxide. *Chemical Society Reviews*. 2013; 42(6): 2423–2436.
36. Zhang, J., Pietro, W. J. and Lever, A. B. P. Rotating ring-disk electrode analysis of $CO_2$ reduction electrocatalyzed by a cobalt tetramethylpyridoporphyrazine on the disk and detected as CO on a platinum ring. *Journal of Electroanalytical Chemistry*. 1996; 403(1–2): 93–100.
37. de Becdelièvre, A. M., de Becdelièvre, J. and Clavilier, J. Electrochemical oxidation of adsorbed carbon monoxide on platinum spherical single crystals: Effect of anion adsorption. *Journal of Electroanalytical Chemistry and Interfacial Electrochemistry*. 1990; 294(1–2): 97–110.
38. Macdonald, D. D. Reflections on the history of electrochemical impedance spectroscopy. *Electrochimica Acta*. 2006; 51(8): 1376–1388.
39. Smith, D. E. Data processing in electrochemistry. *Analytical Chemistry*. 1976; 48(2): 221A–240A.
40. Mcdonald, J. R., ed. *Impedance Spectroscopy: Emphasizing Solid Materials and Systems*. New York: Wiley/Interscience. 1987.
41. Park, S.-M. and Yoo, J.-S. Peer reviewed: Electrochemical impedance spectroscopy for better electrochemical measurements. *Analytical Chemistry*. 2003; 75(21): 455A–461A.

42. Parsons, R. The electrical double layer: Recent experimental and theoretical developments. *Chemical Reviews*. 1990; 90(5): 813–826.
43. Randles, J. E. B. A cathode ray polarograph. Part II. The current–voltage curves. *Transactions of the Faraday Society*. 1948; 44(0): 327–338.
44. Xie, K., Zhang, Y., Meng, G. and Irvine, J. T. S. Electrochemical reduction of $CO_2$ in a proton conducting solid oxide electrolyser. *Journal of Materials Chemistry*. 2011; 21(1): 195–198.
45. Monk, P. M. *Fundamentals of Electroanalytical Chemistry*. Chichester, England: John Wiley & Sons Ltd. 2001.
46. Lu, Q., Rosen, J., Zhou, Y., Hutchings, G. S., Kimmel, Y. C., Chen, J. G. and Jiao, F. A selective and efficient electrocatalyst for carbon dioxide reduction. *Nature Communications*. 2014; 5: 3242.